Communication / Navigation Outage Forecasting System (C/NOFS) Science Plan

The C/NOFS Science Definition Team,
(O. de La Beaujardière, Editor)

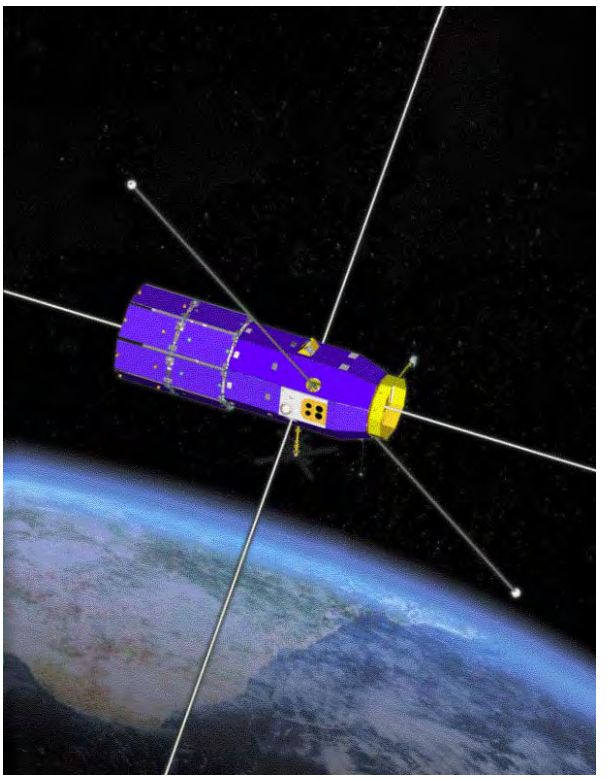

AIR FORCE RESEARCH LABORATORY
Space Vehicles Directorate
29 Randolph Road
Hanscom AFB, MA 01731-3010

- ***How are they structured by bifurcation caused by plasma instabilities?***
- ***How are they sheared by structure in the forces that drive them (e.g., neutral winds), etc.?***

5 Spread-F Irregularities

5.1 Overview and Examples

From the perspective of communication and navigation systems, the most significant feature of the equatorial ionosphere is that it readily becomes unstable after sunset, giving rise to a broad spectrum of irregularities that disrupt radio wave transmissions over a wide range of frequencies. In this section, we briefly describe the irregularities that we expect to measure with the C/NOFS satellite probes and discuss how these data will be characterized to advance our understanding of and ability to predict the unstable equatorial ionosphere significantly.

In order to establish both a causal and a predictive relationship between spread F and communication/ navigation outages, a series of steps must be advanced:

- Characterize the irregularity spectra as a function of their ionospheric driving conditions.
- Understand how the irregularities enable different scattering processes to alter radio wave transmissions (phase, amplitude degradation, etc.) and evaluate the relative efficiencies of these processes as a function of radio frequency or wavelength.
- Predict the occurrence of the irregularities, including their strength and plasma wave characteristics, in order to predict the degree to which they disrupt radio wave communications.

Equipped with a suite of specialized *in situ* and remote sensing instruments, as well as extensive theory and modeling tools, the C/NOFS program has been specifically designed to carry out these steps to advance our understanding of spread-F irregularities.

As mentioned previously, the R-T instability is the primary one at work in the nighttime equatorial ionosphere. R-T develops on the bottomside of the nighttime ionosphere near the magnetic equator and is responsible for the upwelling of depleted flux tubes that “carry” with them a broad spectrum of associated plasma irregularities that evolve as the flux tube rises and bifurcates. These irregularities result from a hierarchy of processes that depend both on their location within the depleted flux tube itself (e.g., along its walls or in the middle of the depletion) and their altitude, since the background neutral density affects the collision and diffusion terms in the dispersion relation.

The irregularities are generally characterized as a broad spectrum of 2D plasma turbulence. The spectral distribution of irregularities includes a broad component associated with waves that have undergone a non-linear cascade process, as discussed in Section 4.4, as well as spectral features associated with drift waves. Current thinking is that structures cascade from large to small scale by a wave-wave coupling mechanism, but drift waves and other distinct instability processes contribute to this distribution of collective unstable scale lengths. Accurate vector electric field and plasma density measurements, such as those available from C/NOFS, will enable the different wave contributions and cross-scale coupling processes to be ascertained for the first time under a wide variety of driving conditions. Ultimately, questions concerning the energy transfer between scale lengths, inverse cascades, and wave anisotropy/isotropy distributions, which are presently not understood, will come

into focus with the advent of the new, comprehensive C/NOFS data set. These new observations will enable us to understand the irregularities at all scales in fundamental new ways.

5.1.1 Fresnel and Bragg Scattering

Beyond characterizing and understanding the plasma irregularities associated with equatorial spread F in the nighttime ionosphere, the next critical step is to understand the various processes that scatter and/or alter radio waves and hence disrupt communication and navigation systems within a wide range of carrier frequencies (wavelengths). For example, the dominant phase scintillation process at work in the spread-F unstable ionosphere is Fresnel scattering. In the Fresnel scatter approximation, plasma density irregularities with horizontal scale lengths of ~100 m in a thin screen at ~400 km altitude contribute the bulk of the weak scatter effects at GHz radio wave frequencies. The shape of the power law spectrum of the irregularities is a critical factor in determining the efficiency and scale lengths of ionospheric scatter via the Fresnel process. Furthermore, although Fresnel scattering for overhead sources is generally caused by a thin layer of horizontally oriented plasma waves, vertically propagating disturbances along the walls of the unstable flux tubes may also give rise to Fresnel scattering affecting, in particular, radio wave sources that are not directly overhead.

Beyond Fresnel scattering, direct Bragg scattering operates when the wavelength of the density irregularity is one half that of the radio wavelength. For HF communications, such scattering occurs at tens of meters, corresponding to scale lengths found in typical spread-F irregularity spectra. In the case of strongly driven spread F, irregularities may be driven to sub-meter scales, implying that it is also possible that Bragg scattering may directly affect radio waves with wavelengths of tens of centimeters, corresponding to frequencies up to a few GHz. Indeed, the frequency spectrum over which Bragg scattering might influence communication and navigation propagation is currently not known, nor is the severity with which such effects might occur.

Data from the C/NOFS satellite will be used to advance our understanding of the degree to which these different scattering mechanisms operate as a function of wavelength.

5.1.2 Direct Observations

To illustrate the type of irregularities and waves that we expect to encounter in the nighttime equatorial ionosphere with the C/NOFS satellite, we present examples from the San Marco satellite and sounding rockets.

5.1.2.1 The San Marco Satellite

Figure 13 depicts 100 seconds of data from the low-inclination San Marco satellite. At ~530 km near 20:30 LT, a strong spread-F plasma depletion was encountered along the satellite track. In the lowest plot, the plasma density decreases by an order of magnitude at 08:56:50 UT and remains quite irregular for a horizontal distance of ~500 km, or until ~08:57:50 UT.

The next two plots above this show the DC electric fields measured by the double probe instrument. In this presentation, the $\mathbf{V} \times \mathbf{B}$ electric fields have been removed and the fields have been rotated into geomagnetic coordinates. In this case, the strong eastward electric fields associated with the plasma depletion correspond to an upwelling of the plasma, and the radially outward component corresponds to a westward plasma drift. The $\mathbf{E} \times \mathbf{B}$ motions of the plasma derived from the DC electric fields are shown in the arrow plots above the DC electric fields. The top plot shows wave electric fields from 7 logarithmically-spaced filter channels between 4 Hz and 1000 Hz. (The filter channel near 24 Hz is not available.) Note the large wave amplitudes at all frequencies that are strongest within, but near the walls of the depletion region. The amplitude of the short scale waves also correlates, to first order, with the amplitude of the DC electric fields.

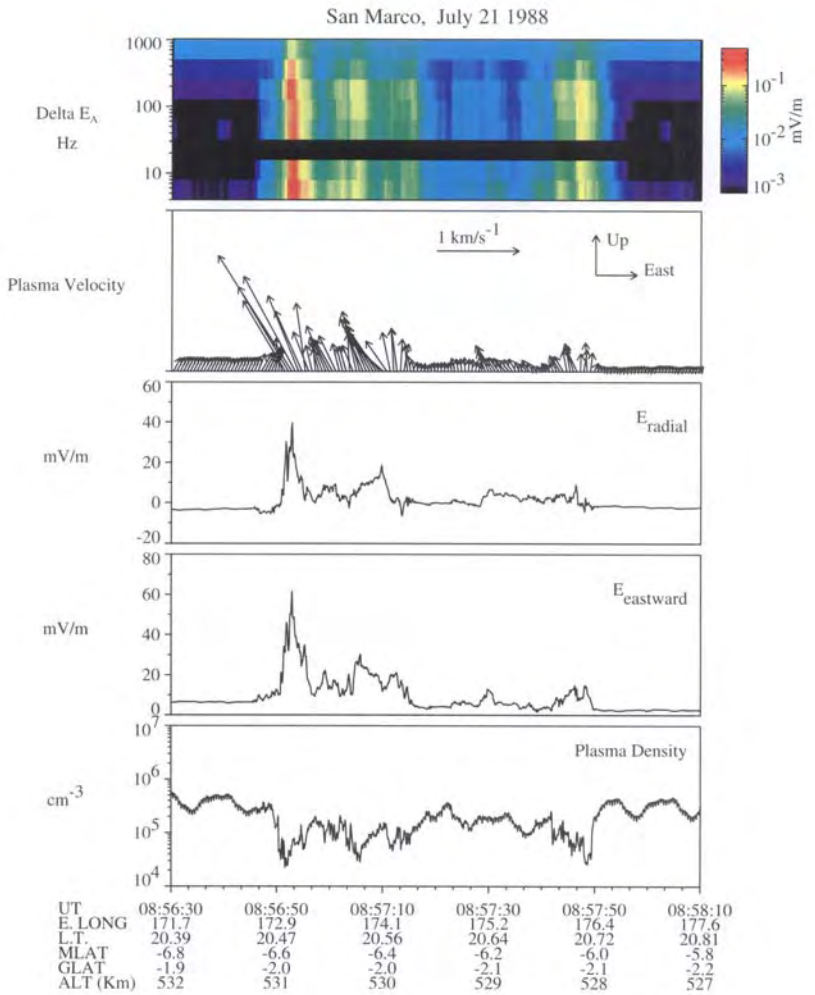

Figure 13. Data from the San Marco satellite showing plasma depletion in the bottom plot with associated radial and zonal DC electric fields in the next two plots. Plasma drifts associated with these electric fields are shown in the fourth plot from the bottom. The top plot shows the wave electric fields within the density depletion. Note that the wave electric fields are strongest where the DC electric fields are strongest, which, in this case, corresponds to regions near the edges of the plasma depletion.

Since the San Marco electric field data were obtained at 8 samples/sec, we can also examine the raw time series data for irregularities up to 4 Hz. Figure 14 shows two orthogonal components of the raw DC electric field data (which include the large sine wave at the vehicle spin rate) from the same event shown in Figure 13. Time series presentations of the wave data from the same channels filtered above 0.4 Hz are also shown in this figure. Since the data were sampled at 8 Hz, the bandwidth of these data ranges from 0.4 – 4.0 Hz. For horizontal waves with essentially zero phase velocity, these frequencies would correspond to wavelengths of 20 – 2 km. However, notice that the intense waves near 172 seconds (which corresponds to 8:56:50 UT) peak at the same time as the large sine wave due primarily to $\mathbf{V} \times \mathbf{B}$ in the raw data peaks.

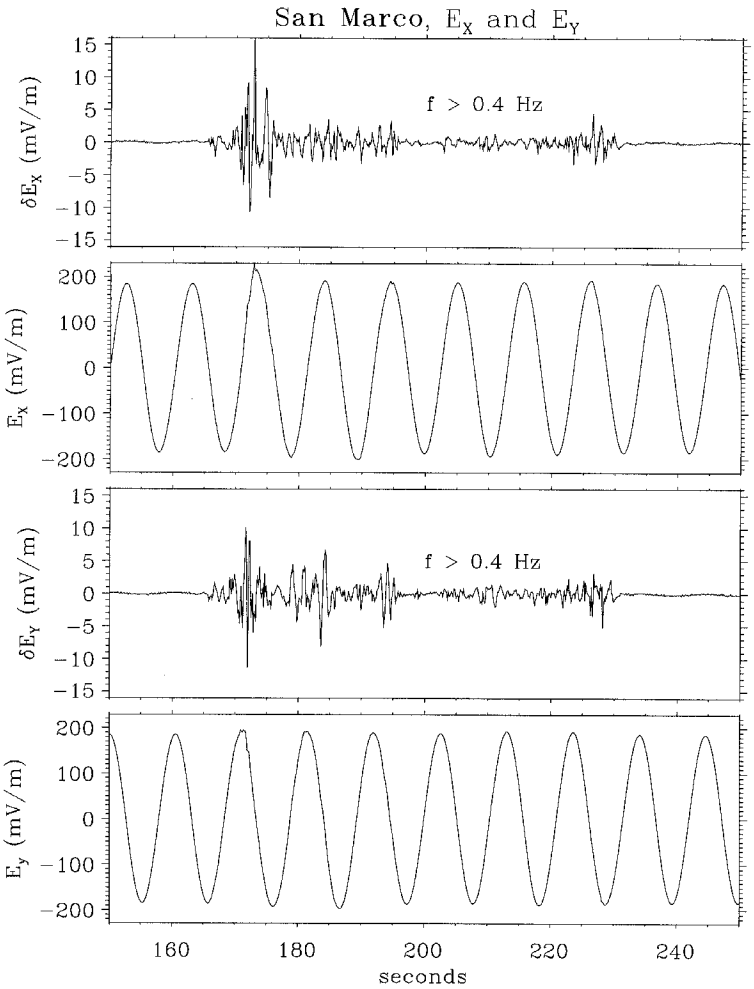

Figure 1b

Figure 14. Raw DC-coupled electric field data for the event shown in Figure 13 plotted with the filtered electric field data in the 0.4 – 4 Hz band. The filtered data show strong wave activity associated with km-scale structures. The large sine wave in the raw data is due to the spin of the San Marco satellite and is 90° out of phase between the two perpendicular electric field components. The amplitude of the large sine wave is mostly due to V x B which is primarily in the radial direction. By comparing the times when the amplitude of the filtered data maximizes with the peaks of the raw DC coupled waveforms, it is shown that the waves include a significant component in the radial direction.

Since $\mathbf{V} \times \mathbf{B}$ is mostly radially outward (as the satellite velocity is horizontal), this clearly indicates that these waves contain a significant component in the *vertical* direction and the wavelengths are actually considerably shorter. Furthermore, the fact that the waves contain a large vertical component immediately demonstrates the presence of large amplitude, long wavelength structures along the walls

of the spread-F depletions. These strong *vertical* wave components have significant consequences for the Fresnel scattering predictions from obliquely oriented plasma density perturbations.

5.1.2.2 Sounding Rockets

We now turn to irregularities measured with probes on sounding rockets in the presence of ESF. Sounding rockets typically have considerably more telemetry than satellites and are able to extend the broadband spectra to higher frequencies. (On C/NOFS, this capability will be afforded by the VEFI burst memory.) Figure 15 shows a sonogram of electric field wave data along with the broadband waves and plasma density from ~480 km to 370 km on the downleg of a rocket experiment flown from Kwajalein Atoll on 2 August 1990. Note that the wave spectra clearly change within the spread-F event, depending on the depth of the plasma density depletion as well as other factors. Since the rocket traveled at speeds ~10 times less than that of an orbiting satellite, the same waves would exist at frequencies ~10 times greater in the satellite reference frame.

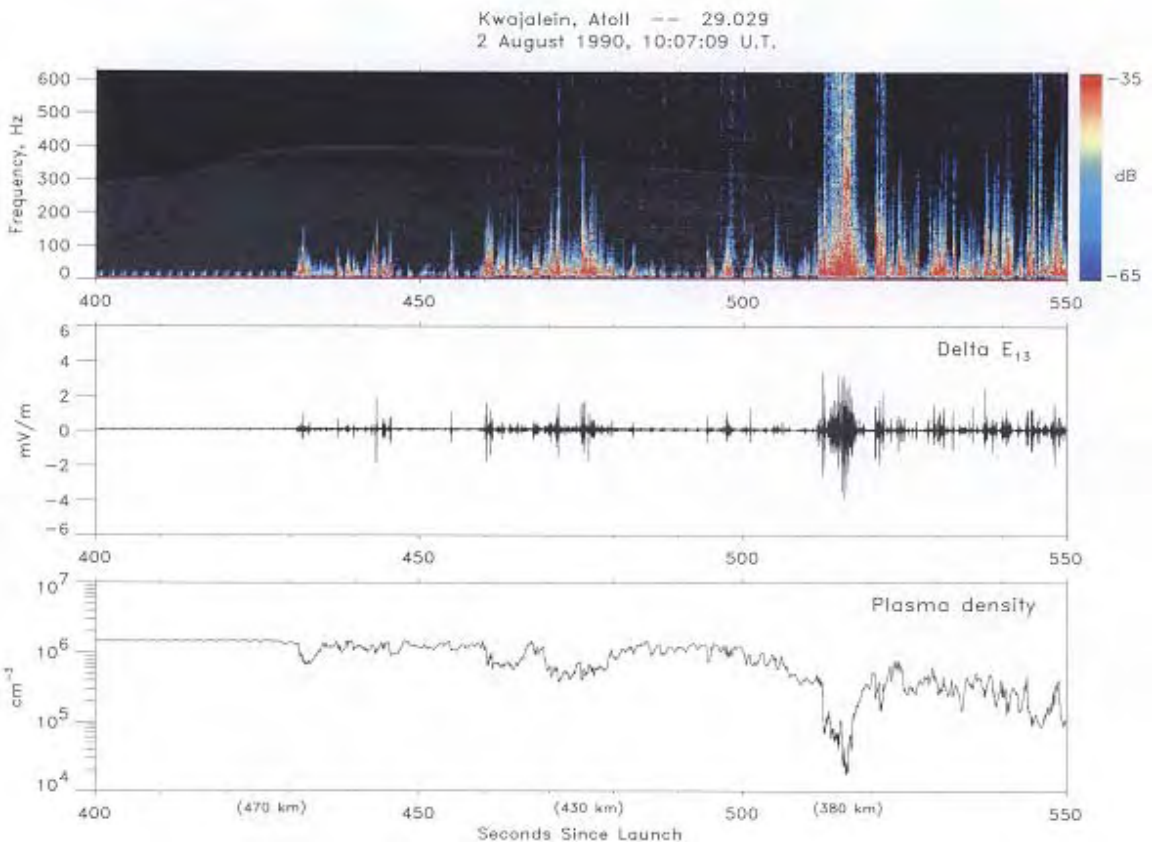

Figure 15. Sounding rocket data from Kwajalein Atoll gathered in the presence of a strong spread-F event. The bottom plot shows the plasma density structure and a large depletion near 515 seconds flight time. The middle plot shows one component of the raw AC electric field data associated with the depletion in the passband of 15 - 625 Hz. The top plot is a spectrogram of the AC electric fields. Note that the irregularity spectrum broadens in the region of the plasma density depletion.

Figure 16 shows a spectrum of electric field irregularities in the deep density depletion near 515.5 seconds at 380 km. Note the enhancement of waves at scales of tens of meters as well as a second peak at tens of cm. Such short scale waves may contribute to Bragg scattering of ~ GHz radio waves. So when the full spectrum of spread-F irregularities is considered, additional scattering mechanisms beyond simple Fresnel scattering must be evaluated to discern the full effect of the irregularities on communication and navigation systems.

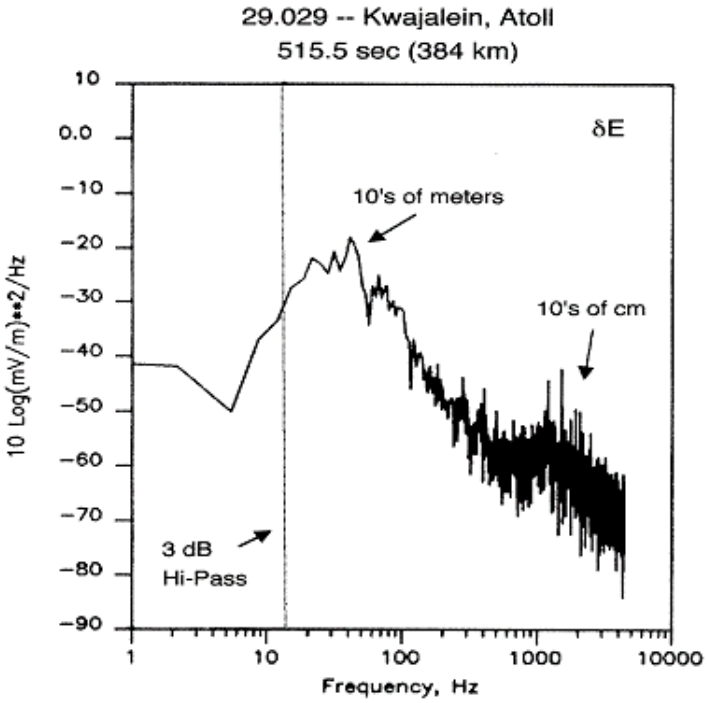

Figure 16. A spectrum of the waves in the plasma density depletion at 515.5 seconds shown in Figure 15. Note the spectral peaks near 50 Hz and 1500 Hz, corresponding to tens of meters and tens of centimeters, respectively. Note that the rocket velocity, which was used to estimate the scales associated with the spectral peaks, is considerably less than that of an orbiting satellite. The AC electric field data shown here underwent a high pass filtering with a 3 dB point at 15 Hz.

Combined electric field and plasma density data from another rocket flight flown during the same campaign from Kwajalein are shown in Figure 17. The uppermost plots show the time series data for the electric and density waveforms, while the middle plots show the power spectral distributions of these waves from ~ 425 to 473 seconds. In these presentations, the *in situ* measured frequency has been converted to wave number simply by using the rocket vehicle speed. Notice that the shape of the δ**E** and δN spectra are similar for long wavelengths, although for wavelengths shorter than those at the spectrum "break" corresponding to 80 m, the δN spectrum falls off more steeply. The δ**E** spectrum thus shows stronger electric field signals at the shorter wavelengths, as expected for cases where δ**E** and δN couple via the Boltzmann relation for shorter scale waves.

The spectra also illustrate a number of outstanding questions in our current understanding of spread F. ***For example, what causes the peak near 1-10 km that is routinely observed in spread F in situ spectra? Similarly, what causes the knee at wavelengths of tens of meters? At what wavelength is the energy injected into the spectrum and where is it dissipated? How does this energy couple***

between scales and at what wavelength regime is this coupling most efficient? Is the bump at tens of centimeters in Figure 16 real, and if so, what causes it?

To answer these questions, detailed wave data gathered as a function of the driving conditions are needed.

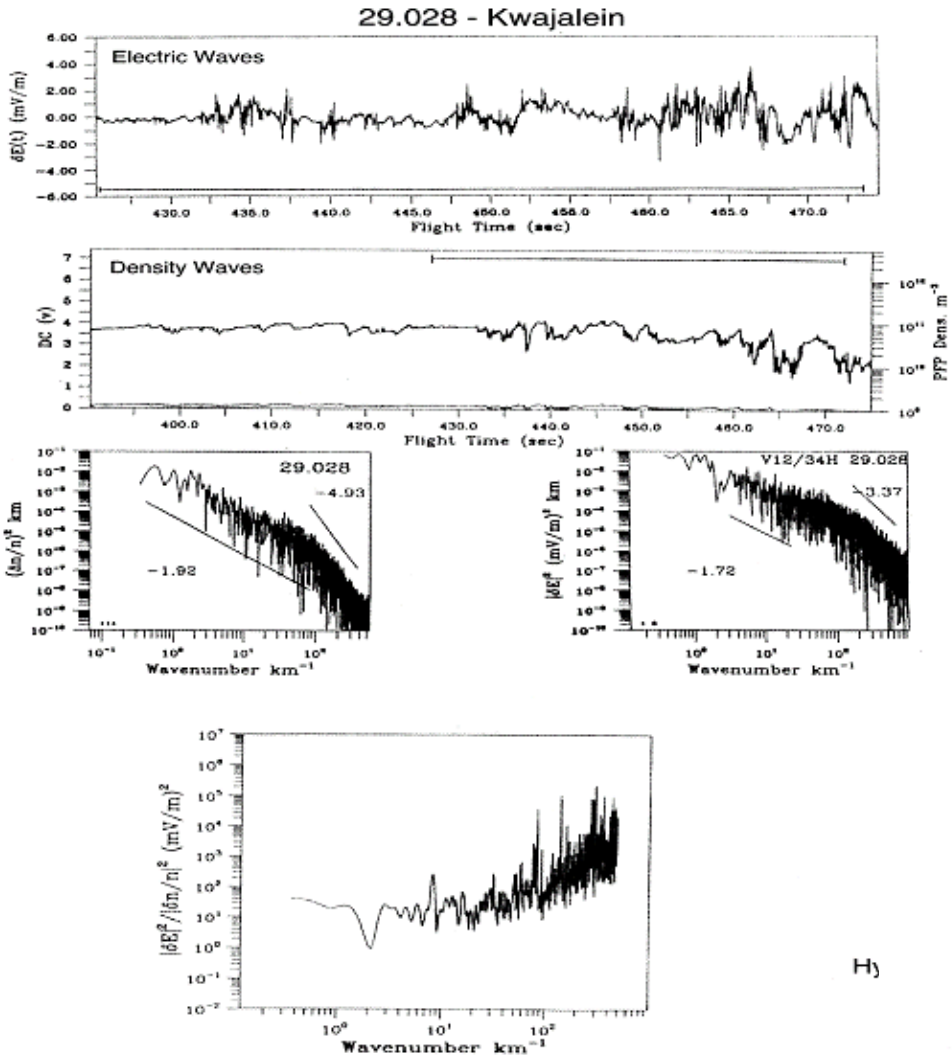

Figure 17. Detailed spectral analysis of AC electric field and plasma density waveforms (top two plots) gathered on a second rocket flight from Kwajalein. The spectra of the density and electric field data are shown below the time series data and reveal similar spectral features for long and medium scale lengths. However, for shorter scale plasma waves < ~50 meters, the density spectrum is much steeper than the electric field spectrum. The lower plot shows the ratio of the two spectra and demonstrates how their spectral features diverge at shorter scales. Figure adapted from *Hysell* et al., [1994].

5.2 Characterization of Irregularities That Cause Spread F

Both plasma density and electric field wave measurements from C/NOFS will be used to characterize the spread-F irregularities that scatter and disrupt communication and navigation signals.

Spread-F irregularities are electrostatic; they contain ΔN and $\Delta\mathbf{E}$ components (in a similar way that electromagnetic waves contain $\Delta\mathbf{B}$ and $\Delta\mathbf{E}$ components). The density component of the irregularities may be directly related to the scattering mechanism that causes scintillations, as it represents the change in the refractive index of the medium through which the waves are propagating. However, since ΔN is a scalar, it contains no information concerning the *direction* of the plasma waves. The electric field wave measurements, on the other hand, provide the direction of the plasma waves since, for the electrostatic case, the direction of the wave vector, **k,** is parallel to $\Delta\mathbf{E}$. The magnitude of **k** is given by $2\pi/\lambda$, where λ is the wavelength. Characterizing the direction of the wave vector, **k**, is essential both for understanding the instability mechanisms that cause the irregularities and also for converting the observed plasma wave frequencies in the satellite frame to wavelengths.

To demonstrate how the plasma wave electric field vector, $\Delta\mathbf{E}$, enables the direction of the plasma waves (and hence their wavelength) to be ascertained, consider Figure 18. The observed frequency of the plasma waves, $\omega_{obs,}$ in the satellite frame is related to the wave vector, **k**, by the equation:

$$\omega_{obs} = \mathbf{k} \cdot \mathbf{V}_{s/c} - \mathbf{k} \cdot \mathbf{V}_{\phi}$$

where $\mathbf{V}$s/c is spacecraft velocity and $\mathbf{V}_{\phi}$ is the wave phase velocity (which is always parallel to **k**).

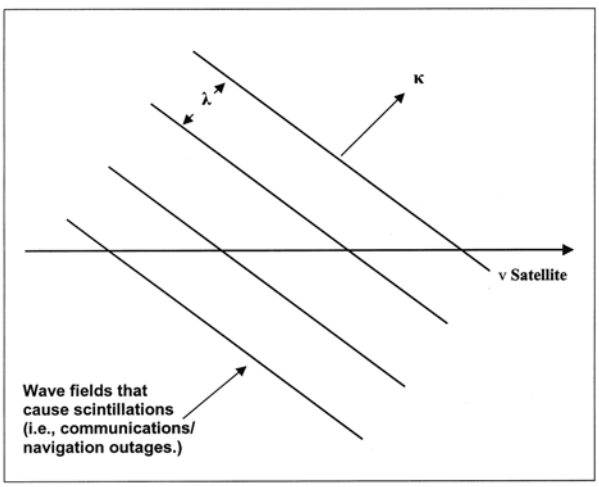

Figure 18. Determination of the direction of the wave vector, k, and conversion of the measured satellite frame frequencies to wavelengths from the measured wave electric field vector, ΔE. See Section 5.2 for details.

To a good first approximation, the wavelength is determined by assuming that the plasma waves are stationary with respect to the spacecraft velocity, or $|\mathbf{V}_{\phi}| << |\mathbf{V}_{s/c}|$. Note, however, that the direction of **k** with respect to the satellite velocity is still needed to convert the observed frequency to a wavelength. To this end, we find the direction of $\Delta\mathbf{E}$ using the vector measurement on C/NOFS, which provides the direction of **k**, since **k** and $\Delta\mathbf{E}$ are parallel for electrostatic waves. Furthermore, the direction of the plasma waves will also be determined as a function of frequency, since shorter scale waves may be traveling at different angles of propagation from the larger scales. Turbulent

wave fields will be characterized by the lack of a well-defined propagation angle, which is an important result necessary for properly interpreting the irregularity spectrum.

Since the direction of the plasma waves is critical to assign a wavelength to the measured frequency, it will be particularly important for revealing the intensity of the plasma waves in directions that are not along the spacecraft velocity, for example, along the depletion walls, which can extend scattering effects beyond those expected for a thin screen. Such vertical and oblique scattering screens may be very effective in causing scintillations for signals propagating at different angles to the observer.

The C/NOFS electric field instrument, VEFI, also includes interferometer channels that permit the direct measurement of the phase velocity of plasma waves as well as direct and more precise measures of their wavelengths. Although $\mathbf{V}_\phi$ is usually considered small compared to the component of the satellite velocity along **k**, $\mathbf{V}_\phi$ may easily be comparable to the **E** x **B** velocity, which for strong spread F and for oblique propagation angles may be significant compared to the satellite velocity component along **k**. The phase velocity provides a direct measure of the dispersion relation and thus provides fundamental understandings of the growth rates, particularly for shorter scale plasma waves.

Instruments on the C/NOFS satellite will provide both the waveforms and spectral characteristics of the density and electric field components of the irregularities that characterize spread F and that directly create the communication and navigation outages in the equatorial ionosphere. As mentioned above, the spectral distributions of the waves can be related to a hierarchy of instabilities and plasma turbulence associated with spread F, for which the main instability mechanism is the R-T instability.

In order to understand the different plasma waves associated with spread F, it is necessary to measure *both* the electric field and plasma density simultaneously to understand their growth and energy sources. This must be done as a function of wavelength and angle with respect to the magnetic field.

The spectral distributions also include contributions from shorter wavelengths (higher frequencies) that are generated via turbulent cascades, drift waves, and other processes. In such cases, the relation of the electric field and the density component of the plasma waves provides important information concerning the wave generation process.

Note from Figure 18 that the electric field spectra are much shallower at the shorter wavelengths than the density spectrum. In these cases, since the density component falls off more steeply, the amount of signal present in the electric field component is much larger and is therefore easier to detect at the shorter scales. Thus, the electric field probes are more sensitive at short wavelengths (< 50 m) and hence will be used to characterize the contributions at shorter scales. For this reason, VEFI will routinely include spectral information at frequencies up to 16 kHz (~0.5 m), with extensions to even shorter scales possible. The shorter scale irregularities may directly scatter and affect radio wave propagation due to Bragg scattering for cases where the cm-scale wavelength is one half that of the direct carrier signal (~GHz frequencies). The complete spectra for electric field and density data will be sampled via the VEFI burst memory and will provide snapshots of the complete wave and spectral characteristics in regions of intense spread F.

By extending the wave measurements to include the shorter scale waves, the measured spectral distributions provide the complete irregularity spectrum. As noted above, they provide evidence for direct scattering processes that are different from those associated with simple Fresnel scattering.

When analyzed as a function of the driving conditions (e.g., DC electric field, plasma density depletion amplitude, altitude, etc.), these spectra are expected to reveal new features of the irregularities themselves and their source mechanisms, providing the necessary understanding to predict their presence in a variety of nighttime ionospheres.

5.3 Using *In Situ* Wave Measurements to Test C/NOFS Predictive Models

C/NOFS wave data will be used to develop and validate predictive models of spread F. C/NOFS instruments measure not only the ionospheric drivers of spread F, but also the spread-F irregularities that scatter radio waves. Thus, by measuring the electric field and plasma density waves that cause the scattering, the predictive models can be directly tested.

For example, consider a case in which data from the C/NOFS instruments are provided to the spread-F models and match conditions that predict the occurrence of intense spread F along the path of the satellite. In this case, we would then use the actual wave measurements to confirm whether spread-F irregularities did occur and at what intensity. The converse is even more interesting. In cases where intense spread-F irregularities are observed *in situ*, we then test the models to learn if they would have predicted the irregularities (amplitude, spectral characteristics, etc.) based on the other C/NOFS measurements of the background drivers.

The first part of the C/NOFS mission will develop our understanding of how spread F is triggered and the irregularities evolve. The plasma wave spectra are vital in this area, as they demonstrate how "active" a given density depletion is in generating plasma waves that might subsequently scatter radio waves. For this reason, we now include the time evolution in the characterization of the plasma depletions and associated irregularities, and thus use the waves to characterize "fresh", "middle-aged", and "old" spread F. All have very different characteristics, particularly with respect to the extent that they cause navigation and communication outages.

Thus, characterizing the irregularities associated with different evolved states of the depletions requires new approaches to advance the predictive capability of the models to a new level.

Finally, there are several scientifically important features of spread F and irregularities that we presently do not understand, but that may become clear with the aid of the data gathered in the C/NOFS investigation. For example, we do not understand at what scale sizes energy is injected and at what scale sizes it is dissipated. ***Further, how does this energy couple between scale sizes, and at what wavelength regime is this accomplished most efficiently?*** We do not understand the peaks in the plasma wave spectra that consistently occur near 1 km or the presence of sub-meter scale waves and whether they are important scatterers for GHz transmissions. By using the wave spectra to examine the whole picture of the spread-F irregularities, we expect to understand the underlying principles of how the irregularities form and, ultimately, how they scatter and disrupt radio wave propagation.

6 Calculating Scintillation Indices from the C/NOFS Data

6.1 Phase Screen Theory

The C/NOFS team elected a phase screen approach to estimate scintillation statistics in both the specification and forecast modes. The limited data available from the spacecraft drive this choice. As the spacecraft passes through an irregularity structure, it provides one-dimensional measurements of the medium. Since scintillations are 3D, largely diffractive phenomena, some method must be used to extend this one-dimensional picture to the other two dimensions.

The phase screen approach is particularly suited to one-dimensional data sets because – at least at the mathematical level – it requires only a one-dimensional parameter if the structures are greatly extended along magnetic field lines. The screen at any one point is characterized by the TEC along

the line-of-sight between orbital and terrestrial transceivers. Since structures in the ionosphere typically drift, the time (or space) evolution of the TEC along this line-of-sight is most useful and constitutes a one-dimensional quantity, NT(x). This quantity is transformed to an equivalent phase shift that is imparted to a uniform plane wave impacting the infinitesimally thin screen at some altitude. The resulting phase perturbations lead to diffraction and amplitude scintillation as the wave passes beyond the screen and propagates to the receiver. The scintillation is computed under a forward-scatter approximation [*Rino*, 1979]. This technique is broadly applicable under ionospheric scintillation conditions, but cannot be used to model multiple-scatter and wide-scatter screen effects.

6.2 C/NOFS Phase Screen Algorithms

To evaluate the line-of-sight-integrated TEC at a given point, it is necessary to know the density structure of the ionosphere along that line-of-sight including, most importantly, the contributions of irregularities. In order to handle this situation in the presence of drift, knowledge of ionospheric densities across an entire plane defined by the drift velocity vector and the line of sight is required. Since neither of these vectors typically lie along the spacecraft path, it is generally necessary to construct density values in the plane based on extrapolation of measured quantities, usually at significant distances from the point of measurement.

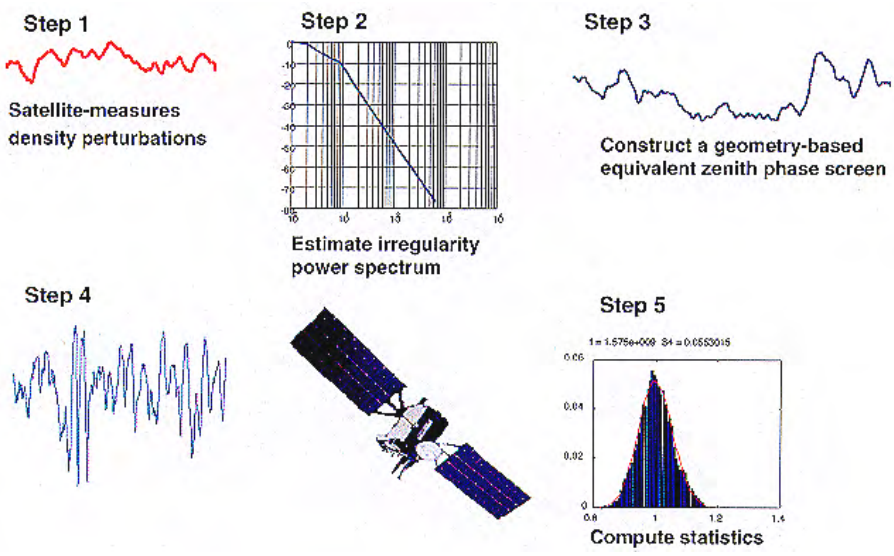

Figure 19. Algorithm for scintillation estimation. Step 1: C/NOFS satellite measures ionospheric density perturbations and returns data to the ground. Step 2: Software is used to estimate the power spectrum of the density irregularities at a given location to help construct a 3D irregularity model for the local ionosphere. Step 3: A thin phase screen is constructed from the irregularity model for a given transmitter-receiver link, converting the geometry to an equivalent zenith screen. Step 4: A signal is propagated through the phase screen to produce a scintillating waveform characteristic of what would be received on the ground. Step 5: Statistics are gathered to determine the estimated strength of amplitude scintillation (S4) seen by a typical receiver.

To handle this problem, we must assume certain models of irregularity homogeneity and anisotropy. Since it is unlikely that the same exact density waveform is duplicated at points far removed from the measurement path, we first characterize the density irregularities measured directly by the satellite by their power spectrum. This effectively throws out the phase information from the Fourier transform

of the density. As seen previously, the power spectrum of the density irregularities takes the form of a two-component power law [*Rufenach*, 1974], with a shallow large-scale regime and a steeper small-scale regime. The spectral break is usually located around the 1-km scale size.

Figure 19 illustrates the steps that are planned to calculate the scintillation parameters. The conversion to power spectra allows us to create different realizations of the irregularity structure while preserving the overall frequency content and distribution. To create a density realization at a given location, we recreate the phase information of the Fourier transform. This is typically accomplished with a random phase function, the most noticeable effect of which is the absence of sharp gradients in the resulting density waveform. It is not known how significantly this loss of structure affects scintillation estimates, apart from a few specific cases.

Once necessary density realizations have been generated, appropriate modifications for the expected correlation lengths (and heights) of the irregularity plume and large-scale irregularity amplitude assumptions can be applied. The best models for these characteristics are not known. The set of density waveforms is finally collapsed into the parameter NT(x), converted to phase angle, and a solution is propagated through the phase screen. Scintillation statistics are gathered from the waveforms produced after propagation through and away from the screen.

6.3 Phase Screen Science Issues

It is important to realize that although certain special cases of scintillation have been observed in practice and adequately modeled using phase screens, there exists no generic engine for turning one-dimensional *in situ* measurements into scintillation estimates. The optimum irregularity models and phase functions are unknown. The dependence of these parameters on background ionization, solar cycle, geomagnetic latitude, season, and transmitter frequency is also unknown.

The operational goal of C/NOFS is to produce scintillation estimates that fit into broad “Red, Yellow, Green” scintillation intensity categories with some fidelity, not to understand the fine time evolution of scintillations observed by a ground station for a given irregularity spectrum. The broader science goal, however, is a better characterization of the effects of the unknowns and an understanding of the physics behind them. This should also improve the “3-bin” estimates and ultimately generate better realizations of the time evolution of scintillating signals. These goals are achievable only within the limits of the information provided on-orbit by the one-dimensional density measurement.

The effort to improve understanding of the sources of scintillations requires a broad spectrum of measurements. ***Can we characterize the transmission medium with sufficient accuracy?*** This is possible using ground-based radar data, such as that from incoherent scatter facilities. Unfortunately, the wavelength-dependent behavior of these measurements renders them incapable of diagnosing the full irregularity spectrum and limits their usefulness to background characterization.

Is it possible to carry out limited tomographic analysis using the transmitters and receivers aboard the C/NOFS spacecraft? It is unlikely that sufficient vertical resolution will be available to model irregularity structures adequately, except in special cases where the CORISS GPS occultation measurements, which can provide information about vertical structure, occur in a region near ground-based CERTO beacon receivers. For the foreseeable future, then, the primary source of data about the irregularities of interest will come from one-dimensional *in situ* measurements (C/NOFS, Republic of China Satellite (ROCSAT)) and the output of physics-based irregularity models. ***Accordingly, emphasis should be placed on enhanced processing techniques for available measurements and improving the suite of diagnostics providing input to the physics-based models.*** Improvements in these models will lead to better 3D specification of irregularity structures and correspondingly improved scintillation estimates.

Additional open questions that bear on the phase screen approximation include the following:

What is the correlation of observed scintillations from LEO beacons with scintillations observed from GEO satellites transmitting through a common volume? This correlation is not well known. ***Scintillations affecting beacons in LEO apply to spherical wave fronts, while those affecting GEO satellites impact largely planar wave fronts. The direct mapping of effects from one case to the other is not understood***. Data from CERTO beacons and GEO spacecraft transmitting through a common volume can be compared to answer this question.

C/NOFS will provide high-resolution electric field measurements. ***Would AC field measurements be useful in estimating density irregularity spectra and thereby predicting scintillations? Would they produce a similar, complementary, or improved approach to scintillation estimation?*** High-resolution electric field data can be used to drive estimation algorithms and test their usefulness.

The effects of amplitude and phase scintillations at different frequencies are known to vary. The thresholds at which each type of scintillation becomes problematic for different applications are largely unknown. Part of the challenge of establishing the long-term usefulness of C/NOFS lies in understanding the required granularity of the specification and forecast products. This effort requires field-testing of a variety of different pieces of equipment in different scintillation environments.

Current research efforts are examining improved techniques for estimating scintillations from limited data sets. Examples of this include discrete versions of the Huygens-Fresnel integrals, improved parabolic equation solvers, and sub-sampled phase screen work. Insights gained from each of these efforts may lead to dramatic improvements in estimation accuracy and efficiency. These techniques can be evaluated in the same manner as the current phase screen approach. Scintillation estimates based on *in situ* data should be compared to measurements by ground facilities to assess each algorithm's performance.

7 Develop Improved Scintillation Climatology

The morphology of equatorial scintillations, based primarily on 250 MHz observations and some 1.5 GHz measurements from geostationary satellites, is well summarized in several publications [*Aarons*, 1982; *Basu and Basu*, 1985; *Aarons*, 1993]. These and other observations have been combined to form an empirical model called WBMOD. The C/NOFS mission offers an opportunity to improve and expand this model.

Recently, a network of SCINDA stations has been deployed in the equatorial region [*Groves et al.*, 1997]. The SCINDA stations perform scintillation and ionospheric drift measurements by the use of 250 MHz transmissions from geostationary satellites. SCINDA also measures scintillations at 1.6 GHz by using transmissions from GPS satellites and at 1.5 GHz (when available) by using transmissions from geostationary satellites. The extensive GHz scintillation measurements with GPS have provided a deeper insight into the earlier scintillation morphology [*Basu and Groves*, 2001].

Equatorial scintillations are nighttime phenomena. The onset of scintillations at the magnetic equator occurs after sunset, with the earliest onset time at ~1900 LT. Scintillations exhibit considerable day-to-day variability and the underlying mechanism of the variability remains unresolved.

The latitudinal extent of equatorial scintillations typically ranges between ~ 15° north and 15° south magnetic latitudes which corresponds to the region between the northern and the southern crests of the equatorial anomaly in F-region ionization. The belt width varies with solar cycle and is generally narrowest during solar minimum and widest in solar maximum. The width also exhibits day-to-day variability. By mapping the extremes of the scintillation belt along magnetic field lines to the

magnetic equator, the altitudinal extent of the irregularities at the magnetic equator can be determined. A scintillation belt width of 15° magnetic latitude corresponds to an altitudinal extent of irregularities to ~750 km above the magnetic equator. Due to a finite upwelling speed of irregularities at the magnetic equator, scintillations near the crest of the anomaly may be delayed by 60 to 90 minutes from their onset at the equator.

The magnitude of amplitude scintillations is expressed by a scintillation index, S4, that is defined by the ratio of the standard deviation of signal intensity fluctuations and the average signal intensity. The index varies from zero to its saturated value that ranges between 1.0 and 1.5. The magnitude of amplitude scintillations decreases with increasing frequency. When scintillations are weak ($S4 < 0.6$), this variation is expressed by $S4 \propto f^{-1.5}$, where f is the frequency. When scintillations are strong, the exponent of the frequency dependence decreases. For operational systems, the depth of fading of the signal intensity in decibels is more useful. For reference it may be noted that 6 dB fading corresponds to $S4 \approx 0.4$, and 12 dB fading corresponds to $S4 \approx 0.7$.

The C/NOFS mission will provide information on how scintillations vary as a function of an extensive set of parameters such as season, solar cycle, magnetic activity, density, electric fields, wind, etc. This climatology will yield valuable relationships as well as quantify the deviations from these average relationships and the expected variability of each parameter.

7.1 Seasonal Effects

The seasonal variation of equatorial scintillations is a function of longitude. At lower frequencies, such as 250 MHz, scintillation activity maximizes in the equinoxes and one of the solstices. Between 80° W and 80° E longitudes, spanning South America and India, scintillation activity is at maximum from September through April including the December solstice. In the Pacific sector, between 100° E and 170° W, spanning the longitudes of the Philippines and Kwajalein Island, the scintillation season covers the equinoxes and the June solstice. Thus, the solsticial patterns in these two sectors are opposite to one another. *Maruyama and Matuura* [1984] suggested that this effect is due to the trans-equatorial wind, which creates an asymmetric electron density variation around the magnetic equator and suppresses the growth of the R-T instability. In order to explain the phenomenon, *Tsunoda* [1985] advanced an alternate hypothesis that irregularities are likely to develop when the longitudinal gradient of magnetic field line integrated Pedersen conductivity is at maximum at the time of sunset. In view of the variation of magnetic declination with longitude, the terminator aligns with the magnetic meridian at different longitudes in different seasons.

This explained the seasonal pattern of scintillations at many longitudes. The problem with the hypothesis is that it does not predict the solsticial asymmetry of scintillations.

At higher frequencies, such as at L-band frequencies, scintillations at all longitudes occur primarily during the equinoxes, and the solsticial activity is either absent or is similar to that of 250 MHz but at a low level. The frequency dependence of the seasonal variation of scintillations is an outstanding issue. ***Are the equatorial irregularities during the solstices weaker than during the equinoxes?***

7.2 Bottomside Sinusoidal Irregularities

It may be mentioned that in addition to plasma bubbles that are caused by the R-T instability [*Ossakow,* 1981] there is a distinct class of equatorial irregularities known as bottomside sinusoidal (BSS) irregularities [*Valladares et al.,* 1983]. The *in situ* density structures of BSS irregularities show a quasi-sinusoidal pattern, and the vertical drifts associated with the irregularities are mostly anti-correlated with the density structures. The one-dimensional spectrum of BSS irregularities is of the

gaussian form with a scale size of ~1 km and not at all similar to the multi-component power law that is associated with EPBs. The BSS irregularities can cause strong VHF scintillations [*Basu et al.*, 1986] but only marginally affect GHz frequencies. These irregularities maximize during solstices, so that in the 250 MHz range, scintillation morphology at an equatorial station is determined by considering occurrence characteristics of both bubble type and BSS irregularities.

Can the C/NOFS observations provide a climatological model for BSS and elucidate mechanisms of BSS formation?

7.3 Explain and Quantify Day to Day Variability

The primary unknown of scintillation morphology is its extreme day-to-day variability. The major scintillation activity in the equatorial region is observed under magnetically quiet conditions. This component is internally driven and cannot be related to external drivers such as solar transients. The day-to-day variability of scintillations needs to be examined in the context of neutral wind variations as detailed in the section on neutral winds. ***C/NOFS will provide the rare opportunity to understand the statistical relationships between irregularities and wind.***

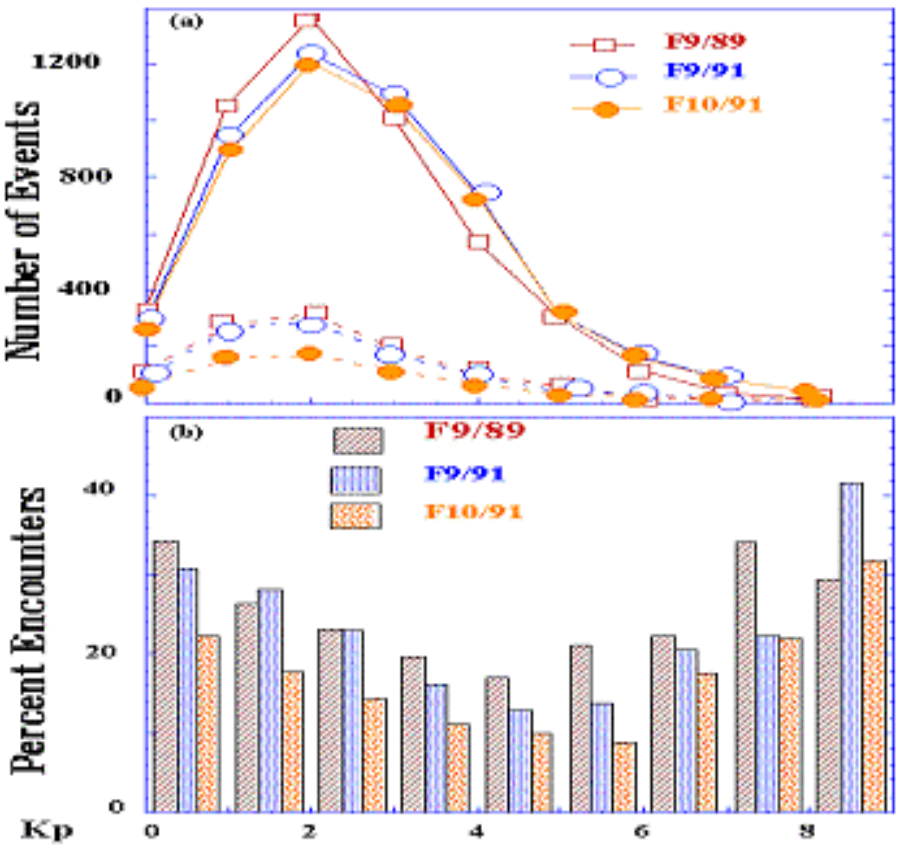

Figure 20. Distributions of EPB encounters as a function of the Kp index. The figure illustrates that the probability of encountering a plasma bubble increases with magnetic activity when Kp > 5. (a) Solid lines plot the number of equatorial crossings while Kp was in a given range. Dashed lines indicate the number of equatorial crossings when EPBs were detected. (b) Histograms give the percent of equatorial

crossings during which EPBs were observed while Kp was in a given range [*Huang et al.*, 2001].

Intense equatorial scintillations are also observed under magnetically active conditions, as illustrated in Figure 20. Although the number of events when Kp is larger than 5 is much smaller than when Kp is low, as shown in the top plot, the probability of encountering EPBs increases with magnetic activity for Kp > 5. Under such externally driven conditions, equatorial scintillations are to be viewed in the context of solar wind-magnetosphere and magnetosphere-ionosphere interactions. The strong modulation by magnetic storm activity was discussed in the sections on magnetic storms and penetration electric fields.

7.4 Solar Cycle Variability

DMSP studies have shown that in all longitude sectors the annual rate of bubble detection is highly correlated with the yearly averaged F10.7 flux [*Huang et al.*, 2002]. Knowing the seasonal patterns of plasma bubble occurrence makes it possible to determine the probability of detecting EPBs at a given longitude from the month and year in the solar cycle. During solar minimum years, the occurrence rate of plasma bubbles is more than an order of magnitude less than at solar maximum. Approximately a third of the EPBs encountered during solar minimum years occurred during intervals when the Dst index was decreasing. Such decreases generally mark periods when the intensity of the ring current is increasing because of the presence of penetration electric fields in the inner magnetosphere, whether or not a magnetic storm occurs.

7.5 Test of Simple Threshold Formulas to Nowcast and Forecast Scintillations

Can simple quantitative empirical thresholds in the equatorial ionosphere be used to forecast scintillations?

Equatorial spread F exists in at least 2 forms: bottomside spread F (BSSF) and bubbles. BSSF is confined to a band ~10° wide near the dip equator that is continuous in LT for many hours (see Figure 21). At high level (strong BSSF) it produces scintillations at VHF and interferes with HF propagation. As bubbles rise in altitude, they extend in latitude and drift eastward, but their LT extent remains small. They produce scintillations at essentially all frequencies if high enough to intersect the high electron density of the equatorial anomaly.

Significant relationships between the phenomena have been observed by *Whalen* [2001, 2002] who found that bubbles can form when the following coincident thresholds are exceeded: maximum prereversal drift velocity of 40 - 50 m/s, anomaly crest maximum latitude at 2100 LT of 15.4° Dip Latitude, anomaly crest N_mF2 of 3.8 x10^6 el/cm^3, appearance of strong BSSF. The drift and BSSF levels are consistent with those found by *Fejer et al.* [1999]. The measurement of any one to be above threshold implies all others are above threshold. Conversely, a measurement that falls below threshold indicates that bubbles will not form. These relations were observed at equinox in the Western American sector during solar maximum. C/NOFS data can be used to determine if these quantitative relationships can serve as scintillation predictors in other seasons, longitudes, and solar cycle conditions.

In another “threshold” study, *Anderson et al.* [2002] found that measuring the height rise with time of the 4 MHz bottomside contour at the magnetic equator provides a very good scintillation “forecast”. If the “average” upward velocity between 18 and 20 LT is greater than 20 m/sec, then the UHF S4 index will be greater than 0.5 90% of the time. Conversely, if it is less than 20 m/sec then S4 will be less than 0.5 90% of the time.

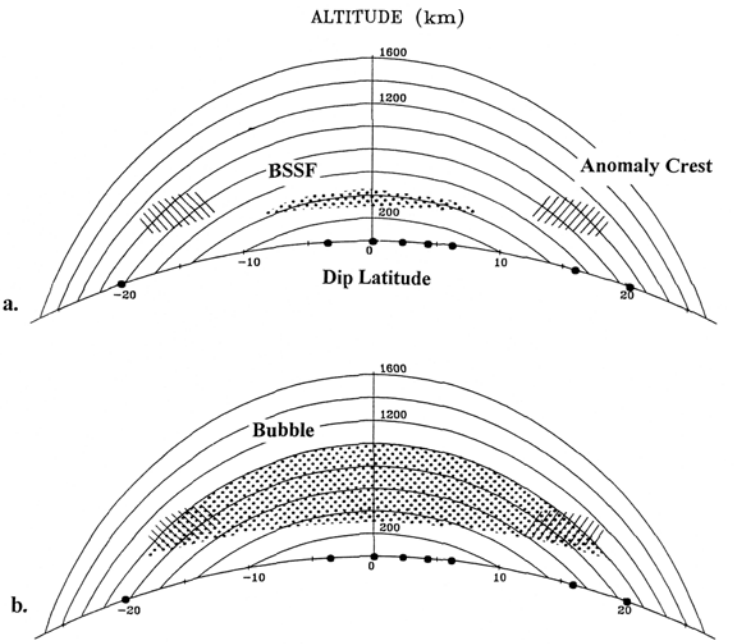

Figure 21. Illustration of the distinction between bottomside spread F (BSSF) and bubbles in latitude and in relation to the geomagnetic field. (a) BSSF (shown with dot pattern) is confined below the F layer maximum and therefore extends via the magnetic field to a narrow band in latitude detectable only by the ionospheric sounders near the dip equator, shown as five solid points. Also shown are the equatorial anomaly crests near ±15° DLAT. Both are continuous in LT, hence in longitude. (b) An EPB, because it rises to high altitude, extends via the magnetic field to high latitude. When it intersects the anomaly above ~16° DLAT it is detectable by the three sounders, two in the north and one in the south. In contrast to BSSF, it is limited in longitudinal width, hence in duration as it drifts overhead to ~1 hour [*Whalen*, 2001].

8 C/NOFS Instrument Development

8.1 Detection of Weak Equatorial Electric Fields

Electric fields of a few mV/m or less will be measured on C/NOFS directly with the three-axis VEFI and indirectly through plasma drifts with IVM. For reference, at the C/NOFS altitude near the magnetic equator, a 1-mV/m electric field produces a plasma drift of ~ 30m/s. These very weak electric fields must be extracted from satellite induced V x B fields >200 mV/m and from unknown DC offsets due to slightly different work function potentials along the active elements of the detectors. To account for satellite motion effects, the attitude of the booms and the spacecraft and the local magnetic field vector must be known to very high precision.

Extracting plasma drifts of a few tens of m/s from the IVM sensor data streams will be equally challenging. The first element of any serious scientific analysis of C/NOFS measurements is the dedication of significant resources to this critical parameter in the first months after launch. Experience teaches that every satellite has its own idiosyncratic effects on plasma measurements. Once these are mastered, the geophysical analysis of measurements usually proceeds smoothly. Data from the Jicamarca radar will be needed to calibrate and validate the quasi DC electric field and plasma drift measurements (see Section 9.1).

8.2 Magnetometer Data

A vector magnetometer will be flown on C/NOFS to assist in the reduction and analysis of VEFI measurements. Errors in standard magnetic field models make it impossible to extract sub-millivolt per meter electric fields from $\mathbf{V}_{sat}$ x $\mathbf{B}$ backgrounds. The magnetometer on C/NOFS has sufficient sensitivity to detect the magnetic deflections caused by the equatorial electrojet. By characterizing the electrojet in the afternoon hours, it may be possible to predict the strengths of electric fields that raise the post-sunset ionosphere. In addition, some bubbles have associated field-aligned currents. The magnetometer will be able to detect Alfvén waves that carry these currents. The presence or absence of these waves distinguishes between bubbles that are actively growing and those near maturity.

8.3 Can the CORISS GPS Receiver Be Used for Scintillation Remote Sensing?

The C/NOFS orbit is such that it will not be able to detect nearby unstable plasmas directly. For example, the spacecraft may be flying above or below a disturbed layer. Under such circumstances CORISS may be able to fill data gaps through remote sensing of turbulence effects. CORISS can be used to identify ray paths from GPS satellites along which scintillations occur which would allow C/NOFS to detect the presence of nearly all EPBs and provide measures of irregularity strength within them. However, the long line-of-sight along the limb view of CORISS renders the geolocation of irregularities difficult. A new technique called diffraction tomography [*Sokolovskiy, et al.,* 2002] offers hope for overcoming this constraint. Phase and amplitude data from the occultation sensor are combined within a back-propagation algorithm to determine the approximate locations of equivalent phase screens responsible for the scintillation. ***Verification and application of the diffraction tomography technique would be quite beneficial for achieving C/NOFS objectives.***

9 Coordinated Ground-Based Measurements

Ground-based instruments play three different roles in the C/NOFS program: (1) to provide real-time data for scintillation and ionospheric models and predictions; (2) to validate AF operational algorithms and calibrate satellite instrumentation; and (3) to support scientific investigations requiring satellite and ground-based observations. Ground-based instruments most relevant to the C/NOFS mission include incoherent scatter radars, coherent scatter radars, digital ionosondes, magnetometers, Fabry-Perot interferometers, and optical imagers. In addition, receivers for GPS, UHF scintillation, and satellite beacons form the backbone of the C/NOFS ground instruments, as mentioned above. Brief descriptions of these instruments and their roles in the C/NOFS mission are given in Section 9.1, while instruments under development are discussed in Section 9.2.

9.1 Jicamarca and Altair Radars

Incoherent scatter radars (ISR) are the most powerful ground-based diagnostic instruments available for measuring the properties of the ionosphere relevant to the C/NOFS mission. ISRs obtain EDPs and ion drifts, as well as ion and electron temperatures. ISRs also provide many parameters needed to determine the motion and development of irregularities and the precursor conditions for the formation of plasma disturbances. All of these measurements are obtained as a function of time and range within the radar beam.

There are three radar facilities in the equatorial latitude belt that are capable of incoherent scatter measurements. One is at Jicamarca (Peru), the second is the Altair radar at Roi Namur (Kwajalein Atoll), the third is in Koto Tabang (Indonesia). Altair and Jicamarca are shown in Figure 22.

Koto Tabang will become operational near the end of 2002. Although it will require long integration times to acquire valid ISR data, Koto Tabang's location at 0.20^o S, 100.32^o E makes these data very useful for C/NOFS. Furthermore, collocated instruments will include an all-sky airglow imager, an airglow photometer, and two GPS receivers.

Figure 22. Altair and Jicamarca incoherent scatter radars.

The critical difference between Jicamarca and Altair is that Jicamarca has a fixed, vertical beam, whereas Altair has a fully steerable dish (see Figure 22). Altair is, therefore, the only place in the world where “time-lapse radar movies” of a large, 3D volume of the ionosphere can be compared to the “snapshots” taken by the C/NOFS satellite. These comparisons will be essential for advancing scientific knowledge of ionospheric plasma phenomenology and for validating the operational forecasts made by the C/NOFS program. These measurements are important for several reasons.

Radars can validate the C/NOFS forecasts. The primary operational product of C/NOFS will be 4- to 6- hour predictions of communication outages and ionospheric plasma disturbances based largely on C/NOFS satellite data. However, because the Earth turns under the orbital track, the satellite will not return to the same region of space in 4 to 6 hours to confirm the predictions. Continuous measurements of ionospheric structures and disturbances above their locations make ground-based radars ideal diagnostic tools for checking and improving the forecast accuracy of C/NOFS.

ISRs can extend the range of application of the forecasts. At a given time, the C/NOFS satellite may not be passing through ionospheric regions needed to predict disturbances near the location of a critical communications link. The orbital track may be displaced in latitude from the site, or the

spacecraft may be at the wrong altitude. The steerable dish at Altair can make 3D maps of the entire ionosphere above Kwajalein with nearly simultaneous measurements at the satellite position and along selected ray paths of interest. Thus, the radar will support extrapolation of forecasts based on localized satellite data to broader geographical regions. These techniques will be tested at Kwajalein and will be applied to all longitudes.

9.1.1 ISR Contributions Toward Operational Ionospheric Forecasting Systems

The success of C/NOFS and follow-on operational systems ultimately depends on how completely we understand the equatorial ionosphere. Many of the research questions outlined in the C/NOFS Science Plan can best be answered by combining the satellite data with observations from ground-based instruments. Jicamarca and Altair provide the most powerful and comprehensive ground-based instruments available in the equatorial region for making these collaborative measurements.

9.1.2 Altair

The scope of Altair contributions to the C/NOFS program will depend on available observing times. Optimum radar usage would include incoherent scatter measurements during the 6 hours between sunset and midnight, when most ionospheric bubbles develop, on days dedicated to C/NOFS support. Altair observations for a few nights each week during dedicated campaigns could be planned. One such campaign is being scheduled for the summer of 2004. For forecast validation in the two years after the C/NOFS launch, less frequent and short duration measurements (e. g., once a week from 19:00 to 22:00 LT) are desired.

All C/NOFS measurements at Altair will be made on a non-interference basis. The details of Altair incoherent scatter operations still must be worked out. Our current understanding is that no modifications to the radar structure, sources, feeds, etc., are necessary. However, additional signal processing and communications equipment may be needed at the radar site.

9.1.3 Jicamarca Radio Observatory

Observations at the Jicamarca Radio Observatory (JRO) have played a crucial role in understanding ESF. In addition to the ISR, shown in Figure 22, collocated instruments at JRO include the SOUSY VHF radar, a digital ionosonde, and a bistatic radar system. The tables in Figure 23 list these radars, and the various operating modes that correspond to scatter modes. In addition, a smaller phased-array ISR of the same design as the Relocatable Atmospheric Observatory (RAO) is planned for 2004. Several optical instruments and a scintillation receiver are located in the vicinity.

The JRO can be run either in incoherent or coherent scatter mode. In incoherent scatter mode the radar provides a measure of the background parameters of the ionosphere such as densities, temperatures, and **E**x**B** drift velocities (see Figure 23, lower table). In coherent scatter mode the measured quantities characterize the statistics of the irregularities rather than the background plasma (see Figure 23, upper table). The Faraday Double Pulse, Vertical, East-West Drift, and Differential Phase modes are also listed. Prior to the onset of spread F, these modes are of particular interest for C/NOFS science. After the onset of spread F, coherent modes such as Interferometry and/or Imaging modes (lower table) become relevant. In special JRO campaigns dedicated to C/NOFS, efforts will be made to use the optimal incoherent and coherent scatter modes as ionospheric conditions toggle between quiescent and disturbed states.

The JULIA mode, labeled interferometry in the Coherent Scatter Modes table, is of particular interest for C/NOFS. JULIA uses low power transmitters and can run unattended, thus providing continuous data at reduced costs. JULIA will provide critical input information for both assimilative and other

forecasting models. Data outputs are in the form of images showing time variations of plumes and irregularities crossing the radar field of view, as shown in Figure 24. With JULIA, it is possible to obtain vertical ionospheric drifts using the 150 km echo technique which has been shown to give the same drifts as the full ISR technique. Since the late afternoon eastward electric field is regarded as the single most important parameter for predicting ESF, this method will be critical for forecasting. Similarly JULIA can be used during the day to determine east-west plasma drifts in the electrojet, which can also be used as a proxy for the eastward electric field. The nighttime JULIA system is also very good for distinguishing bottomside, bottom type, and bubble-related ESF conditions.

Coherent Scatter Modes

Modes	Range (km)	v_z	v_x	ρ	T_e	T_i	N_e	u	v	w
Interferometry	95 – 1500	√ [1]	√							
Imaging	95 – 1500	√ [1]	√					√ [2]		
MST	4 – 85 [3]	√ [1]						√	√	√
Oblique Wide East – West [4]	~105	√						√ [2]		
Oblique Narrow – Wide [4]	95 - 120	√						√ [2]		
Bistatic	95 – 115			√ [5]						
SOUSY MST	4 – 85 [3]	√ [1]						√	√	√

[1] From 150-km echoes only during daytime
[2] In progress….
[3] 25-65 km Stratospheric gap. Mesosphere only daytime.
[4] Wider longitudinal coverage.
[5] Nighttime to be tested

Incoherent Scatter Modes

Modes	Range (km)	v_z	v_x	ρ	T_e	T_i	N_e	u	V_v	w
Faraday Double Pulse	200 – 800	√ [1]		√	√	√	√			
Vertical Drift	200 – 930	√		√ [2]						
East – West Drift	200 – 930	√	√							
Alternating Code	450 – 1400			√ [2]	√	√	√			
Long Pulse	600 – 3000			√ [2]	√	√	√			
Hybrid AC-Faraday	200 – 1400	√ [3]		√	√	√	√			
Differential Phase	90 – 930	√ [3,4]	√ [3]	√ [3]	√ [3]	√ [3]				
SOUSY	200 – 500			√ [5,2]					√ [5]	

[1] From 150-km echoes only daytime
[2] Relative values
[3] In progress…
[4] From EEJ echoes for the lower heights
[5] To be tested

Figure 23. The two tables list the height and parameters that can be obtained from each of the Jicamarca radar operating modes.

Several dedicated projects will be carried out at JRO. As noted above, calibrating DC offsets in the double-probe VEFI experiment on C/NOFS is of very high priority, and JRO is the single most sensitive instrument for this purpose. The eastward electric field can be measured to an absolute accuracy of better than 25 μV/m. The best opportunities for calibration experiments will occur whenever C/NOFS flies within 1°-2° of latitude of the radar beam while crossing the JRO longitude. Regular measurements of the vector electric field by JRO can then be used to calibrate and correct VEFI offsets. These experiments must occur as early as possible in the C/NOFS mission. Seasonal drifts in offset experienced by the double-probe antenna on the San Marco satellite suggest that calibration experiments will be needed for at least a year after launch.

A key question concerns the extent to which the local time variations in electric fields observed at JRO are representative of longitudinal differences. Longitudinal differences in ESF occurrence suggest that the electric field daily variations do depend on longitude. To this end, it will be important to obtain daytime measurements at JULIA while C/NOFS is obtaining data at other longitudes.

The impact of low-altitude velocity shears on the day-to-day variability of ESF may also be important. While such shears cannot be detected by C/NOFS, they can be measured using interferometric techniques within the JULIA beam and/or the JULIA oblique beam. In fact, NASA has planned a rocket campaign for Peru at about the time of the C/NOFS launch, in part to address this issue (see Section 10.2).

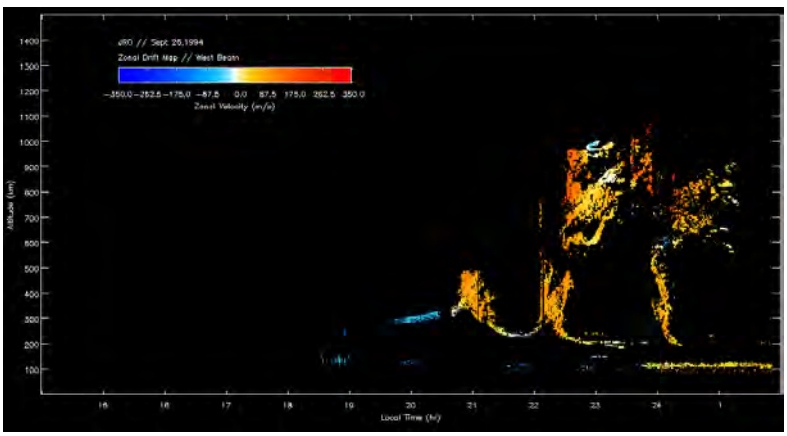

Figure 24. 50 MHz radar interferometer results obtained on September 26-27, 1994 at the Jicamarca Radio Observatory, Peru, near the magnetic equator indicating the distribution of 3-meter irregularities along with their color-coded zonal drifts. The blue colors denote westward drift and red colors indicate eastward drift (*Kudeki et al.*, private communication); for description see *Basu et al.*, [1996].

9.1.4 Other Ground-Based Instruments in South America

There is a vast array of relevant sensors deployed throughout South America, including imagers, Fabry-Perot interferometers (FPIs), radars, and GPS receivers. Measurements from these devices will complement the C/NOFS data and help validate instrument and algorithm operations. For example, Boston College has deployed 5 GPS receivers near the 73° W longitude meridian along the west coast of South America (Figure 25). These receivers measure the variability of latitudinal profiles in TEC (see Figure 26) to determine their effects on the onset and evolution of spread-F plasma structures. The latitudinally distributed GPS receivers also give the amplitude scintillations on a near-real time

basis. The TEC observations allow one to know the maximum latitude to which the irregularities extend and then approximate the maximum altitude of the plasma depletions. Studies based on these receivers, restricted to the 73° W longitude sector, will complement the global C/NOFS mission.

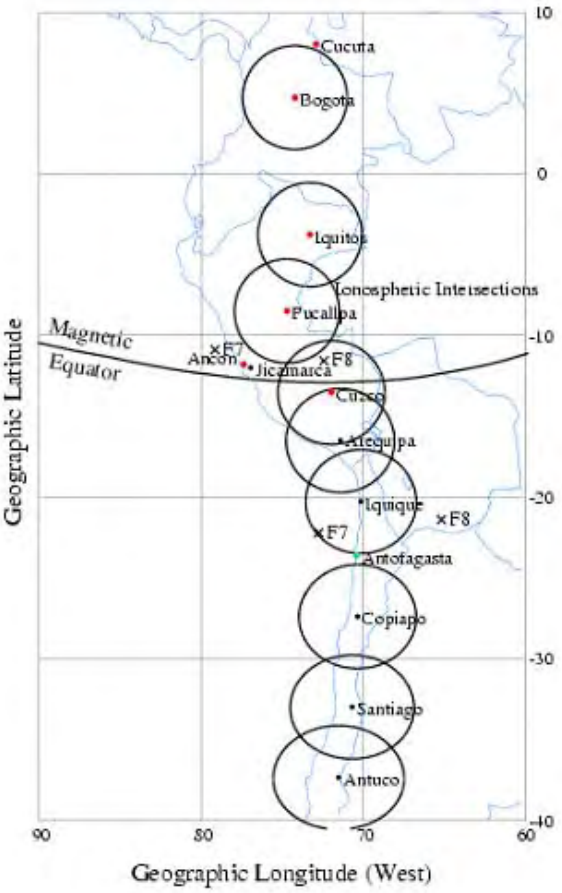

Figure 25. Site locations and field-of-view (40° elevation) of the GPS receivers used to obtain the latitudinal distributions of TEC. The GPS receivers at Bogotá, Iquitos, Pucallpa, Ancon, and Cuzco are operated by Boston College. The receivers at Iquique, Copiapo, and Antuco are part of the SAP (South Andes Project) network and are managed by the University of Hawaii. The receivers at Arequipa and Santiago form part of the IES network [*Valladares et al.*, 2001].

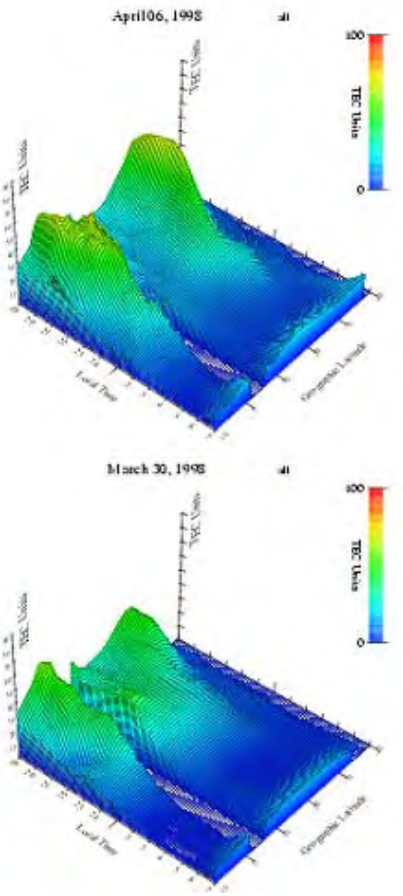

Figure 26. The two plots show 3D views of the TEC values displayed as a function of geographic latitude and local time. TEC values were collected by the chain of GPS receivers in 1998. The top plot corresponds to a night when scintillations were seen at Ancon. The bottom plot is for a night of no scintillations [*Valladares et al.*, 2001].

9.1.5 Pacific Sector

In addition to the SCINDA sites shown in Figure 3, three islands in the Pacific sector will be of great importance for the C/NOFS mission: (1) Hawaii, (2) Christmas Island, at the same longitude but at the magnetic equator, and (3) Pohnpei (Micronesia) also close to the magnetic equator, but three hours earlier in LT.

SRI International has been continuously monitoring ESF from Pohnpei Island for the last two and a half years. SRI has used a 50 MHz radar to obtain maps of backscatter plumes extending up to 1600 km in altitude. The radar also makes electrojet measurements.

In addition, an ionosonde and a magnetometer are located on Pohnpei, and there are plans to install another magnetometer off the equator to monitor the eastward electric field. Finally, oblique-incidence backscattering soundings of both hemispheres will be conducted from Pohnpei (to begin operations in October 2002). These soundings will allow monitoring of the temporal development of both anomaly regions. Thus Pohnpei is one of the best places in the world to collect such comprehensive observations of electrodynamics and ESF.

In Maui, Hawaii, two multi-wavelength cameras are collocated within a large AF telescope on top of the Haleakala volcano. Figure 27 shows images acquired with these two cameras. Remarkably, the equatorial ionosphere is visible from this site. Towering plumes map from 1600 km to ionospheric locations north of Hawaii. Multiple plumes were observed marching eastward across the night sky. The Maui station is permanent and should be used to document ESF activity in the mid-Pacific sector.

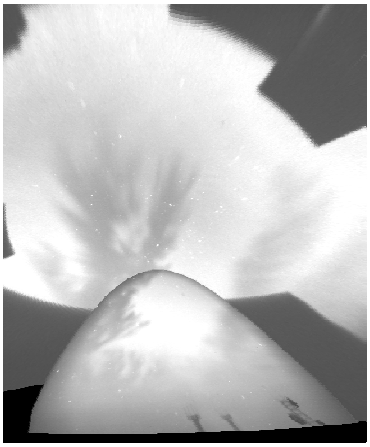

Figure 27. Images taken by two cameras atop the Haleakala volcano in Maui, showing the equatorial ionosphere visible from this site. The lower image is from a narrow-field camera set up to look tangent to field lines at the height of the airglow layer.

Christmas Island already has a 100 m x 100 m antenna array that is virtually identical to the one on Pohnpei. This array is presently used as a wind profiler, but it will be phased out of operation in the near future. It could be used, with some minor modifications, for ESF measurements. Campaigns could then be made jointly with cameras and the radar on Christmas Island.

Plume development on Christmas Island could be compared to that on Pohnpei, which is located three hours in local time to the west of Christmas Island. The pair would provide a unique test bed for equatorial scintillation forecasting algorithms, primarily because they are both located in the Pacific region where the geomagnetic field geometry does not change drastically with longitude. It is, therefore, an ideal place to test forecasting algorithms for predicting the development of ESF.

9.1.6 UHF and GPS Receivers for TEC and L-Band Scintillation Measurements

As mentioned in Section 2.3, scintillation receivers maintained by AFRL are already in place or will soon be deployed near the equator around the globe (Figure 3). They will receive signals from the active CERTO beacon on C/NOFS to specify the degree of UHF phase and amplitude scintillations. In some cases, they are also able to measure scintillations from beacons located on other spacecraft such as the Navy Transit satellites. GPS receivers play a dual role. First, their measurements of TEC are assimilated into the ambient ionospheric model (Section 3.3.1). Second, algorithms applied to GPS signals sampled at 50 GHz estimate the intensity of phase and amplitude scintillations at L-band.

9.2 Instruments under Development

9.2.1 Special Ionosonde For Low Plasma Densities

JRO and Cornell University are planning to deploy a special ionosonde with a large antenna in order to measure the low plasma densities of the nighttime E region. As mentioned in Section 3.2.2, this instrument can provide a measure of the nighttime E-region conductivity at the foot of the equatorial field lines. This crucial parameter for calculating the instability growth rates is presently not known with sufficient precision.

This ionosonde may be located in Piura, Peru, the site of a major university. Piura lies beneath the E-region footprint of field lines that cross the magnetic equator at ~200 km above Jicamarca. This instrument is not expensive, and its deployment merits high priority. Piura has been successfully used to acquire all-sky airglow images and make coherent scatter radar observations of spread F. Note that having several airglow stations would provide 2D or 3D perspectives.

9.2.2 Daytime FPI Measurements

We do not understand the complex electrodynamics of the equatorial ionosphere sufficiently to explain its day-to-day variability. One contributor to this variability is the daily change in semi-diurnal thermospheric tides that modulate zonal thermospheric winds across the dusk terminator. Variations of zonal wind speeds affect the timing and development of the F-region dynamo and, consequently, the growth of plasma irregularities via the generalized R-T instability.

FPIs are used to study thermospheric dynamics by measuring Doppler shifts in 630 nm OI airglow. Thus, FPIs are excellent sensors for observing the speed and flow direction of neutrals in the atmosphere at altitudes between 225 and 275 km. Until recently, such measurements have been confined to the nightside. Extremely bright signals in the Rayleigh-scattered continuum made it impossible to use FPI instruments for daytime measurements.

An instrument called the Second-generation Optimized Fabry-Perot Doppler Imager (SOFDI) is presently being developed at Clemson University. This instrument will be deployed near the magnetic equator at Huancayo, Peru. SOFDI is designed for both night and day time remote sensing of airglow intensities to determine atmospheric winds and temperatures. A unique feature of this instrument is its ability to measure Doppler shifts in four directions simultaneously with articulated telescopes.

The foremost objective proposed for SOFDI is to measure zonal thermospheric winds during the daytime to determine the time of the reversal of zonal thermospheric wind from westward to eastward in late afternoon. One useful study would test the hypothesis that early reversal times indicate a stable F layer that cannot support scintillation activity or ESF disturbances in the evening sector. This hypothesis assumes that early reversal times lead to development of strong eastward thermospheric winds at sunset. The development of an F-region dynamo is inhibited because the conjugate E layer

remains partially sunlit. The associated E-region conductance then shorts out polarization electric fields that otherwise would be produced by the F-region dynamo. Consequently, the vertical ion velocity characterizing the PRE would remain weak and the F layer would be stable. On the other hand, late-time reversals should lead to the production of a strong zonal polarization electric field after E-region plasma has recombined. The **E** x **B** vertical drift activated by this field elevates the F layer to altitudes above 300 km where the growth of the R-T instability can progress rapidly.

9.2.3 Ground-Based Daytime Optical Airglow Studies

An instrument called HIRISE (High Resolution Imaging Spectrograph using Echelle grating) was developed at Boston University to measure daytime airglow emissions. HIRISE is a slit spectrograph capable of making all-sky measurements [*Chakrabarti*, 1998*; Pallamraju et al.*, 2002].

HIRISE measurements have already resolved controversies surrounding the "Ring effect" or filling-in of solar Fraunhofer lines [*Pallamraju et al.*, 2000]. High-latitude observations of OI 630.0 nm red line emissions resulted in the identification of a sunlit auroral arc, corroborated by a concurrently operating incoherent scatter radar [*Pallamraju et al.*, 2001a]. The instrument also measured OI 630.0 nm emissions from the sunlit cusp [*Pallamraju et al.*, 2001b]. Furthermore, daytime red line airglow measurements in Chile demonstrated that dayglow emissions could be used to investigate ionospheric phenomena such as the Appleton anomaly and various waves characteristic of low latitudes. These features show day-to-day variability that correlates with the occurrence/absence of ESF [*Chakrabarti et al.*, 2001]. Thus, HIRISE is capable of identifying ESF precursors in the daytime airglow, which is critical for successful scintillation forecasts.

HIRISE is currently being augmented with multi-wavelength capability. Simultaneous, all-sky images at OI 557.7 and 777.4 nm will augment those at 630.0 nm. Such measurements will shed more light on the altitude variability of upper-atmospheric phenomena and will provide data critical for a comprehensive understanding of ESF.

9.2.4 Tomographic Radio Receiver Array

The University of Illinois at Urbana-Champaign, in collaboration with the Instituto Geofisico del Peru and the JRO, is planning to acquire and deploy a zonal array of TEC receivers across Peru with a base receiver at Jicamarca for radio-tomographic imaging of the equatorial ionosphere [*Kamalabadi et al.*, 2002a]. The array will consist of seven coherent ionospheric Doppler receivers, each capable of receiving transmissions from CERTO.

Tomographic reconstruction techniques will subsequently be used to provide two-dimensional altitude/longitude maps of ionospheric electron density [*Kamalabadi et al.*, 2002b]. The longitudinal coverage crosses Peru roughly along the magnetic equator (-12.5^0 geographic latitude). The array, which includes seven receivers, will constitute the first zonal ionospheric tomography system. It can provide an unprecedented view of the processes responsible for the formation of F-region density structures in equatorial regions.

In addition to providing two-dimensional images of electron density, the receiver array is capable of measuring ionospheric phase scintillations at up to a 1 kHz sampling rate, corresponding to meter-scale range in the F region. Furthermore, the TEC data can be used to augment the radio occultation measurements obtained by CORISS.

10 Observation Campaigns

Observation campaigns are either coordinated with specific ground-based instruments or associated with rocket flights.

10.1 Ground-based Campaigns

Two major campaigns will be carried out in the first eight months. Quite naturally, one will be centered in the 75° West longitude sector where considerable instrumentation already exists. A four-month effort from January through April 2004 will capture the height of the spread-F season as it declines toward equinox in that sector. A key element in this campaign is the instrumentation cluster centered at JRO.

Concerted efforts must be made jointly by the AF, NSF, and NASA to assure adequate support for this instrument set, in addition to those described below. A suitable model is the Thermosphere, Ionosphere, Mesosphere, Energetics and Dynamics (TIMED) mission which pioneered such cooperation.

Key orbits will be those that pass over Jicamarca at ~1700 LT which will reveal the electric field structure characterizing the terminator as it races westward. The goal is to predict the severity of that night's activity, and then to measure that activity using the instrument suite. Equally important will be the ability to check whether the electrical structure of the terminator retains its character as it sweeps over and is observed by JRO.

This sector should also be invaluable for testing whether simple instruments can predict events locally prior to sunset. The most promising in this regard are daytime airglow or TEC measurements of the ratio of anomaly plasma content to the equatorial content. The daytime airglow method of predicting activity has been tested in India with some success. To our knowledge the TEC method has not yet been tried using GPS although it has been proposed for the mid-Pacific sector [*J. Makela, personal communication,* 2001].

A second campaign will center on the mid- to west-Pacific region, from Hawaii to Indonesia. A well-developed suite of instruments already exists including Altair, many airglow images, ionosondes, and GPS receivers. One or more coherent scatter radars, which can give information on the electrical structure at the equator as well as measurements of equatorial F-region irregularities, will be necessary. As noted above, Hawaii is also instrumented to observe the equatorial zone using airglow cameras looking southward and may contribute to predictions for the western Pacific. It is anticipated that Christmas Island will also be well instrumented.

10.2 Rocket Campaigns

One of the chief limitations of the C/NOFS satellite *in situ* data is that they represent a one-dimensional, W-E cut through the equatorial ionosphere. CORISS can make occultation measurements to obtain vertical profiles of electron density at points spaced by ~16° in longitude around the orbit. However, data on the vertical profiles of ion drift, electric fields, density irregularities, and neutral winds are unavailable. The scintillation monitoring ground sites incorporated into C/NOFS do not obtain vertical profile information. Radars, including ionosondes, coherent scatter, and incoherent scatter, certainly provide vertical profile information but not necessarily at the resolution desired (e.g., for density irregularities) or even for all desired parameters (e.g., thermospheric neutral winds).

In order to investigate the vertical profiles of neutral winds and the vertical structure of density irregularities it may be desirable to establish sounding rocket campaigns. Many coordinated rocket and radar studies of ESF have been carried out in Brazil, Peru, Kwajalein, and India [e.g., *Kelley et al.,*

1986, *and references therein; Hysell et al.,* 1994; *Pfaff et al.,* 1997]. Many of these experiments have focused on electron density and electric field measurements and power spectra in developed ESF irregularities. In one experiment of the campaign described by [*Pfaff et al.,* 1997], chemi-luminescent trimethyl aluminum (TMA) trails were released from rockets near dusk to measure neutral winds in the altitude range from 90-180 km. It is not clear how to obtain the neutral wind profile up to the C/NOFS satellite's perigee altitude or during the day, however.

Two areas in which the C/NOFS program stands to gain the most from vertical ionospheric profiling are in knowledge of: (1) the vertical structure of ESF irregularities and associated fields, and (2) the vertical profile of neutral winds. The first addresses the need to understand the three-dimensional disturbance structure for use in forecasting the geographic extent of scintillation effects on the ground. The second presents the possibility that thermospheric neutral wind profiles may be early precursors of ESF activity as many as six hours prior to onset . Rocket experiments have the potential to contribute in both areas.

In addition to the Altair radar, the Army maintains facilities at Roi Namur (Kwajalein Atoll) for building and launching sounding rockets. All of the measurements and experiments outlined in the sounding rocket section of this Science Plan can be carried out at Roi Namur as well as at Punta Lobos, Peru, near Jicamarca.

The first equatorial sounding rocket campaign in many years is planned for March and April of 2004, with more than a dozen rockets to be launched from Punta Lobos, Peru. The Peru campaign is designed to study ESF and mesospheric electrodynamics using sounding rockets in conjunction with JRO. Data from the C/NOFS satellite would contribute to this project by providing an overview of the topside equatorial ionosphere during the campaign.

10.3 Corroborative Satellite Observations

Several satellites will provide observations that will complement the C/NOFS mission. These include DMSP, ROCSAT, TIMED, COSMIC, GRACE, EQUARS, and FalconSat-2 among others. Data from these satellites can be assimilated into the models to validate the C/NOFS-derived parameters and forecast algorithms. By extending the coverage in latitude, longitude, and height, they will also make available more complete ionospheric and thermospheric characterizations. Remote sensing instruments, such as the UV imagers on DMSP and TIMED and the GPS occultation sensors on COSMIC, will be of particular interest due to their wide coverage. In addition, these sensors provide images away from the C/NOFS orbital track and at other local times.

DMSP *in situ* density will contribute the latitudinal extent of EPBs (see Figure 28), as well as the structure (e.g., anomaly peak separation, altitude, asymmetry) of the background F-region ionosphere. High-latitude measurements of particle precipitation, electric fields, and field-aligned currents will be essential to determine the role of magnetospheric effects in triggering and inhibiting ESF and EPBs (see Figure 20).

The ultraviolet sensor on TIMED is the Global Ultraviolet Imager (GUVI), and on DMSP F16-F20 the two sensors are the Special Sensor Ultraviolet Spectrographic Imager (SSUSI) and the Special Sensor Ultraviolet Limb Imager (SSULI). Data from these instruments will provide ionospheric and thermospheric parameters relevant to C/NOFS. The data can be inverted to provide the height and density of the F region maximum, as well as the neutral composition ratio $[O]/[N_2]$.

Figure 29 shows a comparison between observations and climatology. The GUVI limb profiles were taken during a one-day period, and thus are all at the same local time. This figure illustrates the great variability in the Appleton anomaly, both in the data and in the model. The meridional wind affects the asymmetry in the peaks, and the electric field their latitudinal separation. Thus these data could be used

indirectly to estimate the meridional wind and the electric field, as well as to validate the C/NOFS ionospheric models.

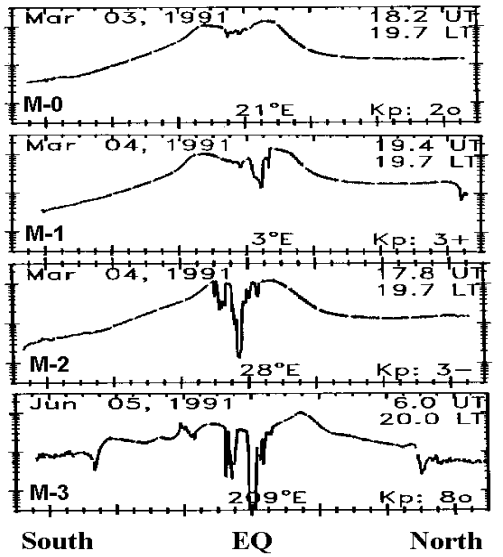

Figure 28. Examples of EPBs observed on DMSP. Plots show ion density (cm^{-3}) as a function of latitude at 20:00 MLT. Several levels of depletions are shown labeled M-0 to M-3 [*Huang et al.*, 2001].

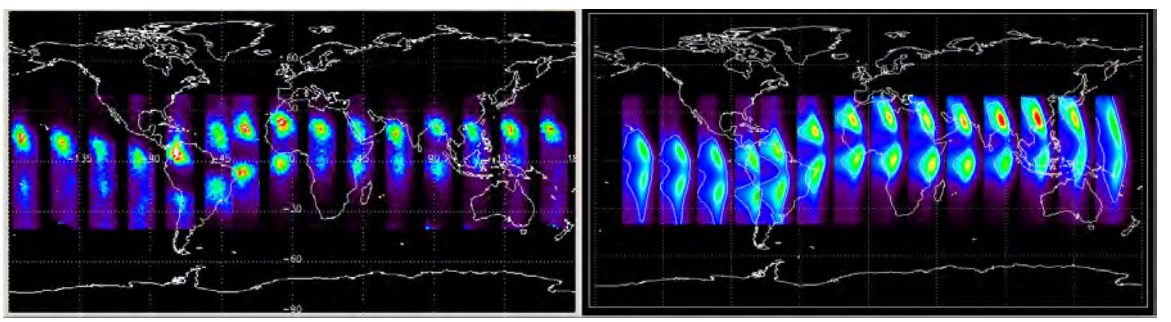

Figure 29. Comparison of GUVI limb profiles with the predictions of the RIBG model. Each individual panel consists of the altitude axis shown horizontally.

Furthermore, the nightside GUVI and SSUSI measurements of the 135.6 nm atmospheric emissions can be used to detect large and small-scale depletions in the ionosphere (see Figure 30). Ionospheric irregularities can be seen as small (6-10 km) enhancements or depletions in the intensity observed in the equatorial ionosphere emissions. Plasma depletions are observed as a reduction of as much as 80% in the observed intensity. The GUVI experiment is able to build up a global map of the distribution of these depletions. The depletions can then be compared to individual C/NOFS passes.

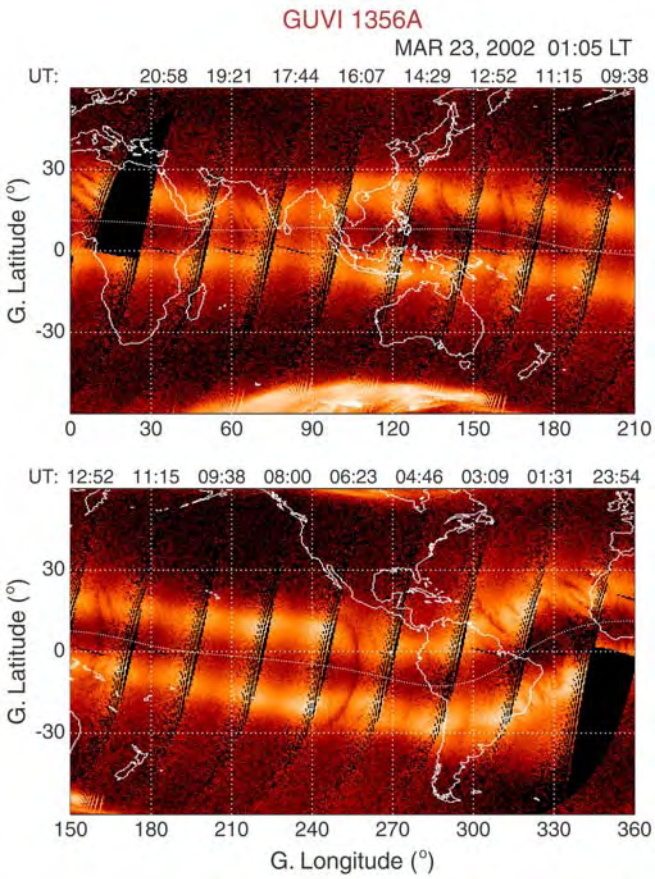

Figure 30. Typical GUVI nightside images of ionospheric irregularity locations.

Sensors on TIMED and DMSP will also provide the solar input in the extreme ultraviolet which is valuable to determine the ion production rate, and thus the electron density profile.

Parameters from other satellites are also of great value for C/NOFS. For example, neutral density measurements from GRACE will help determine the presence of traveling ionospheric disturbances and gravity waves, which play a role in the formation of plasma irregularities. GRACE will also provide an absolute value of the neutral density, an important parameter to quantify the role of thermospheric coupling.

The EQUARS satellite, scheduled for launch in 2006, is a Brazilian satellite to study equatorial irregularities. FalconSat is an AF microsatellite program that will make *in situ* measurements of suprathermal electrons. The primary payload is the Miniature Electrostatic Analyzer (MESA) that will measure electron spectra up to 13 eV.

Since plasma bubbles are approximately field-aligned, simultaneous multi-point measurements of plasma density within a single flux tube will provide insights into spatial structures that may otherwise be ambiguous because temporal effects cannot be separated from spatial effects.

11 Conclusions

The C/NOFS satellite is scheduled to be launched in January 2004 into a low inclination (13°), low altitude elliptical orbit (~400 x 700 km). The satellite instruments include:

- Planar Langmuir Probe (PLP)
- Vector Electric Field Instrument (VEFI)
- Ion Velocity Meter (IVM)
- Neutral Wind Meter (NWM)
- GPS dual-frequency receiver (CORISS)
- Coherent radio beacon (CERTO)

C/NOFS ground-based instruments include SCINDA scintillation receivers as well as GPS receivers to measure TEC and L-Band scintillation. In addition, data from other ground-based instruments such as optical instruments, ionosondes, FPIs, and radars will complement the mission.

The mission profile calls for an initial time in Survey Mode to develop, test, and validate the algorithms, and a second period in Forecast Mode, during which part of the satellite data will be acquired in real time in order to generate specification and forecast maps of the global ionosphere and scintillation levels. The equatorial aeronomy scientific investigations will take place during both Survey and Forecast Modes.

The scientific objectives fall into three categories:

1. Understand the physics of the ionospheric plasma in the equatorial regions. The goal is to specify and forecast the background ionosphere accurately. This implies that the ionospheric drivers – ionospheric as well as thermospheric parameters – need to be specified and forecast.
2. Understand the physical processes that lead to the formation of plasma irregularities in the ionosphere, and identify the mechanisms that trigger or inhibit plasma instability. This goal requires accurate modeling of the parameters that are part of the instability growth rate. The electric field, whether of dynamo or magnetospheric origin, is one of the most important of these parameters. This goal also entails physics-based modeling of plasma bubbles and their time evolution.
3. Characterize ionospheric plasma irregularities and model the propagation of radio waves through the ionosphere in order to estimate the phase and amplitude scintillation for various propagation geometries. This goal requires an understanding of the irregularity spectra and the cascading processes, and the construction of appropriate phase screens.

One of the innovative features of C/NOFS is that most of the scientific effort will be directed towards forecasting. An attempt will be made to forecast ionospheric and plasma irregularities parameters as far as 6 or even 12 hours ahead.

The science objectives cannot be met by using the satellite data alone. Theory and modeling are also required, as well as other satellite and ground-based observations. Synchronized efforts using many instruments, coordinated campaigns, theory, and data analysis are essential.

The maximum benefit can only be met if resources from other agencies such as NSF, NASA, ONR, and AFOSR are applied. In addition, the effort is based on extensive international collaborations. The benefits gained from such synergies have been exemplified on multiple occasions. Recent examples include the Guest Investigator program for the NASA Dynamics Explorer mission, and the TIMED

ground-based component initiative. Multi-instrument studies with C/NOFS will provide results that would be unattainable otherwise. The C/NOFS mission will make available to the scientific community the most extensive set of satellite instruments for the study of equatorial aeronomy to date. This opportunity should not be missed.

The prospects for scientific achievement with C/NOFS are substantial. We anticipate that at the end of the C/NOFS mission, our understanding of the physics of the equatorial ionosphere will have advanced to the point that we can nowcast and forecast the formation of ionospheric irregularities with greatly improved accuracy.

References

Aarons, J., Global morphology of ionospheric scintillations, *Proc. IEEE, 70*, 360, 1982.

Aarons, J., The longitudinal morphology of equatorial *F*-layer irregularities relevant to their occurrence, *Space Sci. Rev., 63,* 209, 1993.

Anderson, D. N., A theoretical study of the ionospheric F region equatorial anomaly, 2. Results in the American and Asian Sectors, *Planet. Space Sci., 21*, 421, 1973.

Anderson, D. N., and M. Mendillo, Ionospheric conditions affecting the evolution of equatorial plasma depletions, *Geophys. Res. Lett., 10*, 541, 1983.

Anderson, D., C. E. Valladares, J. L. Chau, O. Veliz, and B. Reinisch, Forecasting the Occurrence of Ionospheric Scintillation Activity on a Day-to-Day Basis in the South American Sector, Proceedings, Jicamarca 40th Anniversary Workshop, El Pueblo Hotel, Lima, Peru, May 20-23, 2002.

Balsley, B. B., G. Haerendel, and R. A. Greenwald, Equatorial spread *F*: Recent observations and a new interpretation, *J. Geophys. Res., 77*, 5625, 1972.

Barnum, B. H., Electromagnetic and optical characteristics of lightning measured in the earth's ionosphere, Ph.D. thesis, University of Washington, 1999.

Basu, B., Generalized Rayleigh-Taylor instability in the presence of time-dependent equilibrium, *J. Geophys. Res., 102*, 17305, 1997.

Basu, B., Equatorial plasma instability in time-dependent equilibrium, *Phys. Plasmas*, *5*, 2022, 1998.

Basu, B., On the linear theory of equatorial plasma instability: Comparison of different descriptions, *J. Geophys. Res., 107(A8)*, 1199, doi:10.1029/2001JA000317, 2002.

Basu, B., and B. Coppi, Localized plasma depletion in the ionosphere and the equatorial spread *F*, *Geophys. Res. Lett., 10*, 900, 1983.

Basu, B., and B. Coppi, Relevance of plasma and neutral wind velocities to the topology and the excitation of modes for the onset of the equatorial spread F, *J. Geophys. Res., 104*, 225, 1999.

Basu, S., Su. Basu, C. E. Valladares, A. Dasgupta, and H. E. Whitney, Scintillations associated with bottomside sinusoidal irregularities in the equatorial F region, *J. Geophys. Res., 91,* 270, 1986.

Basu, S., et al., Scintillations, plasma drifts, and neutral winds in the equatorial ionosphere after sunset, *J. Geophys. Res.*, 101, *26795*, 1996.

Basu, S., and K. M. Groves, Space Weather, *Geophys. Monograph 125,* 423, 2001.

Basu, Su., and Basu, S., Equatorial scintillations: Advances since ISEA-*6, J. Atmos. Terr. Phys., 47,* 753, 1985.

Biondi, M. A., J. W. Meriwether, Jr., B. G. Fejer, S.A. Gonzales, and D. C. Hallenbeck, Equatorial thermospheric wind changes during the solar cycle: Measurements at Arequipa, Peru, from 1983 to 1990, *J. Geophys. Res., 96*, 15917, 1991.

Burke, W. J., T. L. Aggson, N. C. Maynard, W. R. Hoegy, R. A. Hoffman, R. M. Candy, C. Liebrecht, and E. Rodgers, Effects of a lightning discharge detected by the DE-2 satellite over Hurricane Debbie, *J. Geophys. Res.*, *97*, 6359, 1992.

Burke, W. J., D. R. Weimer, and N. C. Maynard, Geoeffective interplanetary scale sizes derived from regression analysis of polar cap potentials, *J. Geophys. Res.*, *104*, 9989, 1999.

Chakrabarti, S., Ground-based spectroscopic studies of sunlit airglow and aurora, *J. Atmos. Solar-Terr. Phys.*, *60*, 1403, 1998.

Chakrabarti, S., D. Pallamraju, J. Araya, J. Baumgardner, and T. Pedersen, Could post-sunset ionospheric irregularities be predicted using O I 630.0nm daytime airglow, *EOS Trans. AGU*, 82(20) Spring Meet. Suppl., Abstract SA52C-08, 2001.

Eccles, J. V., A simple model of low latitude electric fields, *J. Geophys. Res.*, *103*, 26699, 1998a.

Eccles, J. V., Modeling investigation of the evening prereversal enhancement of the zonal electric field in the equatorial ionosphere, *J. Geophys. Res.*, *103*, 26709, 1998b.

Farrell, W. M., T. L. Aggson, E. B. Rodgers, and W. B. Hanson, Observations of ionospheric electric fields above atmospheric weather systems, *J. Geophys. Res.*, *99*, 19475, 1994.

Farley, D. T., E. Bonelli, B. G. Fejer, and M. F. Larsen, The prereversal enhancement of the zonal electric field in the equatorial ionosphere, *J. Geophys. Res.*, *91*, 13723, 1986.

Fejer, B. G., and L. Scherliess, Empirical models of storm time equatorial zonal electric fields, *J. Geophys. Res.*, *102*, 24047, 1997.

Fejer, B. G., L. Scherliess and E. R. de Paula, Effects of the vertical plasma drift velocity on the generation and evolution of equatorial spread *F*, *J. Geophys. Res.*, *104*, 19859, 1999.

Fuller-Rowell T., and D. Rees, *J. Atmos. Terr. Phys.*, 43, 701, 1981.

Groves, K., et al., Equatorial scintillation and systems support, *Radio Sci.*, *32*, 2047, 1997.

Haerendel, G., and J. V. Eccles, The role of the equatorial electrojet in the evening ionosphere, *J. Geophys. Res.*, *97*, 1181, 1992.

Hedin, A. E., N. W. Spencer, and T. L. Killeen, Empirical global model of upper thermosphere winds based on Atmosphere and Dynamics Explorer satellite data, *J. Geophys. Res.*, *93*, 9959, 1988.

Helliwell, R. A., *Whistlers and related ionospheric phenomena*, Stanford University Press, Palo Alto, California, 1965.

Hocke, K., and T. Tsuda, Gravity waves and ionospheric irregularities over tropical convection zones observed by GPS/MET radio occultation, *Geophys. Res. Lett.*, *28*, 2815, 2001.

Holzworth, R. H., R. M. Winglee, and M. C. Kelley, Whistler waves in the high-latitude magnetosphere, *J. Geophys. Res.*, *104*, 17369, 1999.

Huang, C. Y., W. J. Burke, J. S. Machuzak, L. C. Gentile, and P. J. Sultan, DMSP observations of equatorial plasma bubbles in the topside ionosphere near solar maximum, *J. Geophys. Res.*, *106*, 8131, 2001.

Huang, C. Y., W. J. Burke, J. S. Machuzak, L. C. Gentile, and P. J. Sultan, Equatorial plasma bubbles observed by DMSP satellites during a full solar cycle: Toward a global climatology, *J. Geophys. Res.*, *107(A12)*, 1434, doi: 10.1029/2002JA009452, 2002.

Huba, J., and G. Joyce, SAMI3: A 3-D Model of the low and mid latitude ionosphere, IES Symposium, 2002.

Hysell, D. L., M. C. Kelley, W. E. Swartz, and D. T. Farley, VHF radar and rocket observations of equatorial spread *F* on Kwajalein, *J. Geophys. Res.*, *99*, 15065, 1994.

Kamalabadi, F., S. Franke, E. Kudeki, P. Tzanos, P. Bernhardt, C. Siefring, and I. Galysh, Two-dimensional imaging of equatorial spread-F bubbles with a longitudinal radio receiver array, Proceedings, Jicamarca 40th Anniversary Workshop, El Pueblo Hotel, Lima, Peru, May 20-23, 2002a.

Kamalabadi, F., G. Bust, K. Dymond, S. Gonzalez, P. Bernhardt, S. Chakrabarti, D. Cotton, A. Stephan, R. McCoy, S. Budzien, S. Thonnard, Tomographic studies of aeronomic phenomena using radio and UV techniques, *J. Atmos. Terr. Phy.*, *64*, 1573, 2002b.

Kelley, M. C., M. F. Larsen, C. LaHoz, and J. P. McClure, Gravity wave initiation of equatorial spread F: A case study, *J. Geophys. Res.*, *86*, 9087, 1981.

Kelley, M. C., et al., Electrical measurements in the atmosphere and the ionosphere over an active thunderstorm 1. Campaign overview and initial ionospheric results, *J. Geophys. Res.*, *90*, 9815, 1985.

Kelley, M. C., J. LaBelle , E. Kudeki, B. G. Fejer, Sa. Basu, Su. Basu, K. D. Baker, C. Hanuisse, P. Argo, R. F. Woodman, W. E. Swartz, D. T. Farley, and J. W. Meriwether, Jr., The Condor equatorial spread *F* campaign: Overview and results of the large-scale measurements, *J. Geophys. Res.*, *91*, 5487, 1986.

Kelley, M. C., *The Earth's Ionosphere*, Academic Press, Inc., 1989.

Kelley, M. C., In situ ionospheric observations of severe weather-related gravity waves and associated small-scale plasma structure, *J. Geophys. Res.*, *102*, 329, 1997.

Li, Y., Electrical and optical phenomenon over thunderstorms, Ph.D. thesis, University of Washington, 1993.

Maruyama, T., and N. Matuura, Longitudinal variability of annual changes in activity of equatorial spread *F* and plasma bubbles, *J. Geophys. Res.*, *89*, 10903, 1984.

Mendillo, M., J. Baumgardner, X. Pi, P. J. Sultan, and R. Tsunoda, Onset conditions for equatorial spread *F*, *J. Geophys. Res.*, *97*, 13865, 1992.

Mendillo, M., J. Meriwether, and M. Biondi, Testing the thermospheric neutral wind suppression mechanism for day-to-day variability of equatorial spread *F*, *J. Geophys. Res.*, *106*, 3655, 2001.

McClure, J. P., S. Singh, D. K. Bamgboye, F. S. Johnson, and H. Kil, Occurrence of equatorial *F* region irregularities: Evidence for tropospheric seeding, *J. Geophys. Res.*, *103*, 29119, 1998.

Nishida, A., Geomagnetic DP 2 fluctuations and associated magnetospheric phenomena, *J. Geophys. Res.*, *73*, 1795, 1968.

Ossakow, S. L., Spread-*F* theories – a review, *J. Atmos. Terr. Phys.*, *43*, 437, 1981.

Ott, E., Theory of Rayleigh-Taylor bubbles in the equatorial ionosphere, *J.* Geophys. *Res.*, *83*, 2066, 1978.

Pallamraju D., J. Baumgardner, and S. Chakrabarti, A multiwavelength investigation of the Ring effect in the day sky spectrum, *Geophys. Res. Lett.*, *27*, 1875, 2000.

Pallamraju, D., J. Baumgardner, S. Chakrabarti, and T. R. Pedersen, Simultaneous ground based observations of an auroral arc in daytime/twilighttime O I 630.0 nm emission and by incoherent scatter radar, *J. Geophys. Res.*, *106*, 5543, 2001a.

Pallamraju, D., S. Chakrabarti, J. Baumgardner, and T. R. Pedersen, Ground-based spectroscopic observations of O I 630.0 nm daytime aurora from Sondrestrom fjord in Greenland, *EOS Trans. AGU*, 82(20) Spring Meet. Suppl., Abstract SA41A-03, 2001b.

Pallamraju, D., J. Baumgardner, and S. Chakrabarti, HIRISE: A ground-based High Resolution Imaging Spectrograph using Echelle grating for measuring daytime airglow and auroral emissions, *J. Atmos. Solar-Terr. Phys.*, *64*, 1581, 2002.

Pfaff, R. F., J. H. A. Sobral, M. A. Abdu, W. E. Swartz, J. W. LaBelle, M. F. Larsen, R. A. Goldberg, F. J. Schmidlin, The Guará campaign: A series of rocket-radar investigations of the Earth's upper atmosphere at the magnetic equator, *Geophys. Res. Lett.*, *24*, 1663, 1997.

Prakash, S., Production of electric field perturbations by gravity wave winds in the *E* region suitable for initiating equatorial spread *F*, *J. Geophys. Res.*, *104*, 10051, 1999.

Raghavarao, R., L. E. Wharton, N. W. Spencer, H. G. Mayr, and L. H. Brace, An equatorial temperature and wind anomaly (ETWA), *Geophys. Res. Lett.*, *18*, 1193, 1991.

Raghavarao, R., W. R. Hoegy, N. W. Spencer, and L. E. Wharton, Neutral temperature anomaly in the equatorial thermosphere - A source of vertical winds, *Geophys. Res. Lett.*, *20*, 1023, 1993.

Rino, C. L., A power law phase screen model for ionospheric scintillation, *Radio Sci.*, *14*, 1135, 1979.

Rishbeth, H., The *F*-Layer Dynamo, *Planet. Space Sci*., *19*, 263, 1971.

Rottger, J., Equatorial spread-*F* by electric fields and atmospheric gravity waves generated by thunderstorms, *J. Atmos. Terr. Phys.*, *43*, 453, 1981.

Rufenach, C. L., Wavelength dependence of radio scintillation: Ionosphere and interplanetary irregularities, *J. Geophys. Res.*, *79*, 1562, 1974.

Scherliess, L., and B. G. Fejer, Storm time dependence of equatorial disturbance dynamo zonal electric fields, J. Geophys. Res., 102, 24037, 1997.

Schunk, R. W., J. J. Sojka, and V. Eccles, Expanded capabilities for the ionospheric forecast model, Final Report AFRL-VS-HA-TR-98-0001, 1997.

Singh, S., F. S. Johnson, and R. A. Power, Gravity wave seeding of equatorial plasma bubbles, *J. Geophys. Res.*, *102*, 7399, 1997.

Sekar, R., and M. C. Kelley, On the combined effects of vertical shear and zonal electric field patterns on nonlinear equatorial spread *F* evolution, *J. Geophys. Res.*, *13*, 20735, 1998.

Sokolovskiy, S., W. Schreiner, C. Rocken, and D. Hunt, Detection of high-altitude ionospheric irregularities with GPS/MET, *Geophys. Res. Lett.*, *29*, 3-1, doi: 10.1029/2001GL013398, 2002.

Sultan, P. J., Linear theory and modeling of the Rayleigh-Taylor instability leading to the occurrence of equatorial spread *F*, *J. Geophys. Res.*, *101*, 26875, 1996.

Tsunoda, R. T., Control of the seasonal and longitudinal occurrence of equatorial scintillations by the longitudinal gradient in integrated *E* region Pedersen conductivity, *J. Geophys. Res.*, *90*, 447, 1985.

Ushio, T., S. J. Heckman, D. J. Boccippio, H. J. Christian, and Z. I. Kwasaki, A survey of thunderstorm flash rates compared to cloud top height using TRMM satellite data, *J. Geophys. Res.*, *106*, 24089, 2001.

Valladares, C. E., W. B. Hanson, J. P. McClure, and B. L. Cragin, Bottomside sinusoidal irregularities in the equatorial *F* region, *J. Geophys. Res.*, *88*, 8025, 1983.

Valladares C.E., S. Basu, K. Groves, M.P. Hagan, D. Hysell, A. J. Mazzella, Jr., R. E. Sheehan, Measurement of the latitudinal distributions of total electron content during equatorial spread *F* events, *J. Geophys. Res*., 106, 29133, 2001.

Whalen, J. A., The equatorial anomaly: Its quantitative relation to equatorial bubbles, bottomside spread *F* and E × B drift velocity during a month at solar maximum, *J. Geophys. Res.*, *106*, 29125, 2001.

Whalen, J. A., Dependence of equatorial bubbles and bottomside spread *F* on season, magnetic activity, and E × B drift velocity during solar maximum, *J. Geophys. Res.*, *107(A2)*, doi: 10.1029/2001JA000039, 2002.

Woodman, R. F., and E. Kudeki, A causal relationship between lightning and explosive spread *F*, *Geophys. Res. Lett.*, *11*, 1165, 1984.

Zalesak, S. T., S. L. Ossakow, and P. K. Chaturvedi, Nonlinear equatorial spread F: The effect of neutral winds and background Pedersen conductivity, *J. Geophys. Res.*, *87*, 151, 1982.

Acronyms

AC	Alternating current
ACE	Advanced Composition Explorer
AF	Air Force
AFOSR	Air Force Office of Scientific Research
AFRL/VS	Air Force Research Laboratory Space Vehicles Directorate
ASC	All-sky camera
BSS	Bottomside sinusoidal
BSSF	Bottomside Spread F
CERTO	Coherent Electromagnetic Radio Tomography
CINDI	Coupled Ion Neutral Dynamics Investigation
C/NOFS	Communication / Navigation Outage Forecasting System
CORISS	C/NOFS Occultation Receiver for Ionospheric Sensing and Specification
COSMIC	Constellation Observing System for Meteorology, Ionosphere, and Climate
CRRES	Combined Release and Radiation Effects Satellite
CTS	Cross Track Wind Sensor
DC	Direct current
DMSP	Defense Meteorological Satellite Program
EDP	Electron Density Profile
EPB	Equatorial plasma bubble
EQUARS	Equatorial Atmosphere Research Satellite
ESF	Equatorial Spread F
EUV	Extreme ultraviolet
FPIs	Fabry-Perot interferometers
GEO	Geosynchronous orbit
GPS	Global Positioning System
GRACE	Gravity Recovery and Climate Experiment
GSFC	Goddard Space Flight Center
GUVI	Global Ultraviolet Imager
HF	High frequency
HIRISE	High Resolution Imaging Spectrograph using Echelle grating
IDM	Ion Drift Meter
IEF	Interplanetary electric field
IFM	Ionospheric Forecast Model
IMF	Interplanetary magnetic field
ISR	Incoherent scatter radar
IVM	Ion Velocity Meter
JRO	Jicamarca Radio Observatory
JULIA	Jicamarca Unattended Long-term investigations of the Ionosphere and Atmosphere
LD	Lightning detector
LEO	Low Earth orbit
MESA	Miniature Electrostatic Analyzer
MSFM	Magnetospheric Specification and Forecast Model
NASA	National Aeronautics and Space Administration
NRL	Naval Research Laboratory
NSF	National Science Foundation
NWM	Neutral Wind Meter

ONR	Office of Naval Research
PLP	Planar Langmuir Probe
PRE	Prereversal enhancement
RAO	Relocatable Atmospheric Observatory
RF	Radio frequency
ROCSAT	Republic of China Satellite
RPA	Retarding Potential Analyzer
R-T	Rayleigh-Taylor
RWS	Ram Wind Sensor
SAP	South Andes Project
SCINDA	Scintillation Network Decision Aid
SOFDI	Second-generation Optimized Fabry-Perot Doppler Imager
SOUSY	SOUnding SYstem for atmospheric structure and dynamics
SSULI	Special Sensor Ultraviolet Limb Imager
SSUSI	Special Sensor Ultraviolet Spectrographic Imager
TDRSS	Tracking and Data Relay Satellite System
TEC	Total Electron Content
TFM	Thermospheric Forecast Model
TIMED	Thermosphere, Ionosphere, Mesosphere, Energetics, and Dynamics
TMA	Trimethyl Aluminum
UHF	Ultra high frequency
UV	Ultraviolet
VEFI	Vector Electric Field Instrument
VHF	Very high frequency

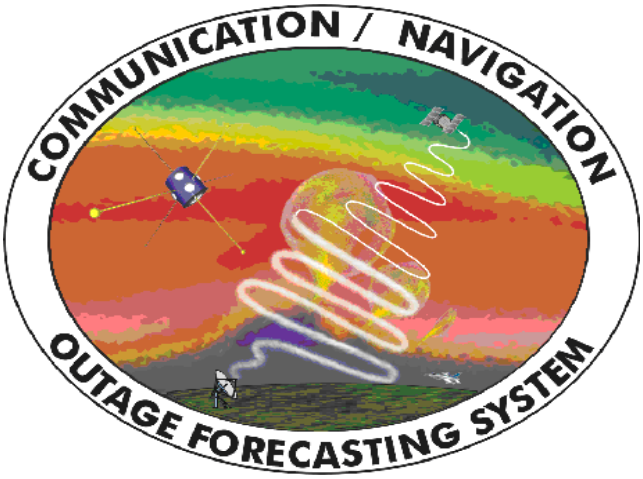
COMMUNICATION / NAVIGATION
OUTAGE FORECASTING SYSTEM